



1 **Secondary ice production processes in wintertime alpine**
2 **mixed-phase clouds**

3

4 Paraskevi Georgakaki¹, Georgia Sotiropoulou^{1,2}, Étienne Vignon³, Anne-Claire Billault-
5 Roux⁴, Alexis Berne⁴ and Athanasios Nenes^{1,5}

6

7 ¹Laboratory of Atmospheric Processes and their Impacts, School of Architecture, Civil & Environmental
8 Engineering, École Polytechnique Fédérale de Lausanne, Lausanne, CH-1015, Switzerland

9 ²Department of Meteorology, Stockholm University & Bolin Center for Climate Research, Stockholm, Sweden

10 ³Laboratoire de Météorologie Dynamique/IPSL/Sorbonne Université/CNRS, UMR 8539, Paris, France

11 ⁴Environmental Remote Sensing Laboratory, School of Architecture, Civil & Environmental Engineering, École
12 Polytechnique Fédérale de Lausanne, Lausanne, CH-1015, Switzerland

13 ⁵Center for Studies of Air Quality and Climate Change, Institute of Chemical Engineering Sciences, Foundation
14 for Research and Technology Hellas, Patras, GR-26504, Greece

15 *Correspondence to:* athanasios.nenes@epfl.ch

16

17 **Abstract**

18 Observations of orographic mixed-phase clouds (MPCs) have long shown that measured ice
19 crystal number concentrations (ICNCs) can exceed the concentration of ice nucleating particles
20 by orders of magnitude. Additionally, model simulations of alpine clouds are frequently found
21 to underestimate the amount of ice compared with observations. Surface-based blowing snow,
22 hoar frost and secondary ice production processes have been suggested as potential causes, but
23 their relative importance and persistence remains highly uncertain. Here we study ice
24 production mechanisms in wintertime orographic MPCs observed during the Cloud and
25 Aerosol Characterization Experiment (CLACE) 2014 campaign at the Jungfraujoch site in the
26 Swiss Alps with the Weather Research and Forecasting model (WRF). Simulations suggest
27 that droplet shattering is not a significant source of ice crystals at this specific location – but
28 break-up upon collisions between ice particles is quite active, elevating the predicted ICNCs
29 by up to 3 orders of magnitude, which is consistent with observations. The initiation of the ice-
30 ice collisional break-up mechanism is primarily associated with the occurrence of seeder-feeder
31 events from higher precipitating cloud layers. The enhanced aggregation of snowflakes is found
32 to drive secondary ice formation in the simulated clouds, the role of which is strengthened
33 when the large hydrometeors interact with the primary ice crystals formed in the feeder cloud.
34 Including a constant source of cloud ice crystals from blowing snow, through the action of the
35 break-up mechanism, can episodically enhance ICNCs. Increases in secondary ice fragment
36 generation can be counterbalanced by enhanced orographic precipitation, which seems to
37 prevent explosive multiplication and cloud dissipation. These findings highlight the importance
38 of secondary ice and “seeding” mechanisms – primarily falling ice from above and to a lesser



39 degree blowing ice from the surface – which frequently enhance primary ice and determine the
40 phase state and properties of MPCs.

41

42 **1. Introduction**

43 Understanding orographic precipitation is one of the most critical aspects of weather
44 forecasting in mountainous regions (Roe, 2005; Rotunno and Houze, 2007; Chow et al., 2013).
45 Orographic clouds are often mixed-phase clouds (MPCs), containing simultaneously
46 supercooled liquid water droplets and ice crystals (Lloyd et al., 2015; Lohmann et al., 2016;
47 Henneberg et al., 2017). In mid- and high-latitude environments almost all precipitation
48 originates from the ice phase (Field and Heymsfield, 2015; Mülmenstädt et al., 2015),
49 highlighting the importance of correctly simulating the amount and distribution of both liquid
50 water and ice (i.e., the liquid-ice phase partitioning) in MPCs (Korolev et al., 2017).

51 Our understanding of MPCs remains incomplete owing to the numerous and highly
52 nonlinear cloud microphysical pathways driving their properties and evolution (Morrison et al.,
53 2012). Due to the lower equilibrium water vapor pressure over ice crystals than over liquid
54 water, MPCs tend to glaciate over time through the Wegener-Bergeron-Findeisen (WBF)
55 process, which is the rapid ice crystal growth at the expense of the surrounding evaporating
56 cloud droplets (Bergeron, 1935; Findeisen, 1938). Another process that can trigger cloud
57 glaciation and has been shown to enhance precipitation over mountains is the seeder-feeder
58 mechanism (e.g., Roe, 2005). This mechanism has been observed in several field studies (e.g.,
59 Reinking et al., 2000; Purdy et al., 2005; Mott et al., 2014; Ramelli et al., 2021) and refers to
60 ice crystals falling from a high-level seeder cloud into a lower-level cloud (external seeder-
61 feeder event) or a lower-lying part of the same cloud (in-cloud seeder-feeder event), where they
62 act as seeds for the glaciation of clouds. Satellite products covering the 11-year period between
63 April 2006 and October 2017 indicated that seeding events are widespread over Switzerland,
64 occurring with a frequency of 31% of the total observations (Proske et al., 2021). Despite these
65 two mechanisms that can readily destabilize an orographic cloud, a high frequency of MPCs
66 have been reported under high updraft velocity conditions prevailing over the complex
67 mountainous terrain (e.g., in the Swiss Alps), where supercooled liquid droplets are generated
68 faster than depleted by depositional ice growth and riming, leading to persistent mixed-phase
69 conditions (Korolev and Isaac, 2003; Lohmann et al., 2016).

70 At temperatures between 0 °C and –38 °C, where mixed-phase conditions can occur,
71 primary ice formation in clouds is catalyzed by the presence of insoluble aerosols that act as



72 ice nucleating particles (INPs) (e.g., Hoose and Möhler, 2012, Kanji et al., 2017). However,
73 in-situ observations of MPCs forming over mountain-top research stations or near mountain
74 slopes regularly reveal that there is a mismatch between the scarcity of primary INPs and the
75 measured ice crystal number concentrations (ICNCs) – the latter being several orders of
76 magnitude more abundant (Rogers and Vali, 1987; Geerts et al., 2015; Lloyd et al., 2015; Beck
77 et al., 2018; Lowenthal et al., 2019; Mignani et al., 2019). Model simulations of alpine MPCs
78 frequently fail to reproduce the elevated ICNCs dictated by observations (Farrington et al.,
79 2016; Henneberg et al., 2017; Dedekind et al., 2021). The fact that primary ice cannot explain
80 the observed ICNCs in orographic MPCs has often been attributed to the influence of surface
81 processes such as the lofting of snowflakes (i.e., blowing snow; Rogers and Vali, 1987; Geerts
82 et al., 2015), detachment of surface hoar frost (Lloyd et al., 2015), turbulence near the mountain
83 surface or convergence of ice particles due to orographic lifting (Beck et al., 2018) and riming
84 on snow-covered surfaces (Rogers and Vali, 1987).

85 Among these surface processes, the impact of blowing snow ice particles (BIPS) has been
86 studied thoroughly, either using observations collected in mountainous regions (e.g., Lloyd et
87 al., 2015; Beck et al., 2018; Lowenthal et al., 2019), and detailed surface snow models (e.g.,
88 Lehning et al., 2006; Vionnet et al., 2013, 2014) or through remote sensing techniques (e.g.,
89 Rogers and Vali, 1987; Vali et al., 2012; Geerts et al., 2015). BIPS are found to hover close to
90 the surface provided that the wind speed exceeds a threshold value, which varies between 4
91 and 13 ms^{-1} (e.g., Déry and Yau, 1999; Mahesh et al., 2003), depending on the snowpack
92 properties and the prevailing atmospheric conditions. The transport of BIPS is commonly
93 separated into the saltation layer and the turbulent suspension layer. The saltation layer is a
94 shallow layer formed close to the ground, where the transported ice particles are found to follow
95 ballistic trajectories. Turbulent eddies or upward gusts can then diffuse the saltated ice particles
96 up to a height of several tens of meters above the surface, into the suspension layer (e.g., Vali
97 et al., 2012; Vionnet et al., 2014).

98 In-cloud secondary ice production (SIP) processes may also enhance ice production after
99 the initial primary ice nucleation events. Especially for orographic clouds, whose cloud top
100 temperatures are not cold enough to activate sufficient INPs, ice multiplication through SIP
101 might be particularly important. Over the past few decades, several SIP mechanisms have
102 emerged in literature, a detailed review of which is provided by Field et al. (2017) and Korolev
103 and Leisner (2020). We briefly review the three main SIP mechanisms below.

104 The rime-splintering, also known as the Hallett-Mossop (HM) process (Hallett and
105 Mossop, 1974), is argued to be the most efficient one in slightly supercooled clouds (i.e.,



106 temperatures warmer than $-10\text{ }^{\circ}\text{C}$). The HM process refers to the ejection of small secondary
107 ice splinters after a supercooled droplet with a diameter larger than $\sim 25\text{ }\mu\text{m}$ rimes onto a large
108 ice particle at temperatures between -8 and $-3\text{ }^{\circ}\text{C}$ (Choulaton et al., 1980; Heymsfield and
109 Mossop, 1984). Although this is the only SIP mechanism widely implemented in current
110 microphysics schemes (e.g., Beheng, 1987; Phillips et al., 2001; Morrison et al., 2005), recent
111 modeling studies of slightly supercooled polar clouds, have shown that it cannot sufficiently
112 explain the enhanced ICNCs in remote environments (Young et al., 2019; Sotiropoulou et al.,
113 2020, 2021a). Moreover, aircraft measurements have reported high ICNCs when the conditions
114 required for HM initiation are not fulfilled (e.g., Korolev et al., 2020).

115 A second process that is found to contribute to ice multiplication over a wider
116 temperature range is the collisional breakup (BR), which involves the fracturing of delicate ice
117 particles due to collisions with other ice particles (Vardiman, 1978; Griggs and Choulaton,
118 1986; Takahashi et al., 1995). Evidence for this process is provided from several field studies
119 in the Arctic (Rangno and Hobbs, 2001; Schwarzenboeck et al., 2009) or in the Alps (Mignani
120 et al., 2019; Ramelli et al., 2021) and from limited laboratory investigations (Vardiman 1978;
121 Takahashi et al. 1995). These two studies created a basis for various numerical formulations of
122 the BR mechanism (e.g., Phillips et al., 2017a; Sullivan et al., 2018a; Sotiropoulou et al., 2020).
123 Parameterizations of this mechanism are implemented in small-scale models (Fridlind et al.,
124 2007; Phillips et al., 2017a, b; Sotiropoulou et al., 2020, 2021b; Sullivan et al., 2018a; Yano
125 and Phillips, 2011; Yano et al., 2016), mesoscale models (Hoarau et al., 2018; Sullivan et al.,
126 2018b; Qu et al., 2020; Sotiropoulou et al., 2021a; Dedekind et al., 2021) and global climate
127 models (Zhao and Liu, 2021). These modeling studies followed several approaches to
128 implement the effect of BR. For instance, Hoarau et al. (2018) assumed a constant number of
129 fragments generated per collision in the Meso-NH model, while Sullivan et al. (2018b)
130 implemented a temperature-dependent relationship in the COSMO-ART mesoscale model
131 based on the results of Takahashi et al. (1995). This simplified formulation was further
132 modified to account for the hydrometeor size scaling, which improved the representation of
133 ICNCs in alpine clouds (Dedekind et al., 2021). Sotiropoulou et al. (2020) and (2021a)
134 reproduced the observed ICNCs in polar clouds, by applying the physically-based
135 parameterization developed by Phillips et al. (2017a, b). At slightly colder temperatures
136 (between $-12.5\text{ }^{\circ}\text{C}$ and $-7\text{ }^{\circ}\text{C}$), however, BR was found to be generally weak over the Arctic
137 (Sotiropoulou et al., 2021b; Zhao et al., 2021).

138 Droplet shattering (DS) during freezing is a third process that is frequently suggested to
139 explain the unexpected ice enhancement in clouds. This mechanism occurs when a drizzle-



140 sized droplet, with a diameter larger than $\sim 50 \mu\text{m}$ collides with an ice particle or INP, triggering
141 its freezing after a solid ice shell is formed around the droplet (e.g., Griggs and Choulaton,
142 1983). As the freezing moves inward, the pressure starts to build and the freezing droplet reacts
143 by either breakup in two halves, cracking, bubble burst or jetting (e.g., Keinert et al., 2020).
144 These processes may be accompanied by the ejection of small ice fragments, the number of
145 which is yet poorly constrained as recent laboratory studies are showing a large diversity of
146 results (Lauber et al., 2018; Keinert et al., 2020; Kleinheins et al., 2021). Individual
147 experiments of freezing droplets reported the maximum fragmentation rate at temperatures
148 between ~ -10 and $-15 \text{ }^\circ\text{C}$ (Leisner et al., 2014; Lauber et al., 2018; Keinert et al., 2020). DS
149 is found to be very efficient in vigorous convective updrafts (Lawson et al., 2015; Phillips et
150 al., 2018; Korolev et al., 2020; Qu et al., 2020), while remote sensing observations indicate that
151 DS can be much more conducive to SIP in slightly supercooled Arctic MPCs than the well-
152 known HM process (Luke et al., 2021). This is in line with single-column simulations
153 performed by Zhao et al. (2021), but contradicts the findings of small-scale modeling studies
154 suggesting that DS is ineffective in polar regions (Fu et al., 2019; Sotiropoulou et al., 2020).
155 Mesoscale model simulations of winter alpine clouds formed at temperatures lower than $-8 \text{ }^\circ\text{C}$
156 indicate that DS is not contributing to the modeled ICNCs (Dedekind et al., 2021), while field
157 observations suggest the increasing efficiency of the mechanism at temperatures warmer than
158 $-3 \text{ }^\circ\text{C}$ (Lauber et al., 2021).

159 In the orographic MPCs observed during the Cloud and Aerosol Characterization
160 Experiment (CLACE) 2014 campaign at the high-altitude research station of Jungfraujoch
161 (JFJ) in the Swiss Alps, the measured ICNCs exceeded the predicted INPs by 3 orders of
162 magnitude, reaching up to $\sim 1000 \text{ L}^{-1}$ at temperatures around $-15 \text{ }^\circ\text{C}$ (Lloyd et al. 2015). Whilst
163 ice multiplication through BR and DS mechanisms show a peak production around a similar
164 temperature, Lloyd et al (2015) did not find evidence for their occurrence. Instead, they
165 suggested that at periods when there was a strong correlation between horizontal wind speed
166 and observed ICNCs, BIPS is contributing to the latter, but the mechanism was incapable of
167 producing ICNCs higher than $\sim 100 \text{ L}^{-1}$. In the absence of such correlation, a flux of hoar frost
168 crystals was considered responsible for the very high ice concentration events (ICNCs > 100
169 L^{-1}), albeit without any direct evidence. Beck et al. (2018) argued that the relationship between
170 ICNCs and horizontal wind speed may not be a good indicator for distinguishing between
171 blowing snow and hoar frost. Their measurements conducted at the Sonnblick Observatory in
172 the Austrian Alps revealed the presence of several hundred ice crystals of blowing snow per
173 liter during cloud-free conditions. In a cloudy environment, though, such high contribution



174 from BIPS was found only close to the surface, with the concentrations dropping to several
175 tens to 100 L^{-1} at heights above $\sim 10 \text{ m}$.

176 From a modeling perspective, the causes of the surprisingly high ICNCs in orographic
177 MPCs formed during the CLACE 2014 campaign were explored in Farrington et al. (2016).
178 Since temperatures at JFJ are generally outside the HM temperature range ($< -8 \text{ }^\circ\text{C}$), Farrington
179 et al. (2016) used back trajectories analysis to investigate whether splinters produced at lower
180 altitudes through the HM process could be lifted to the summit of JFJ elevating the modeled
181 ICNCs. They showed that the inclusion of the HM process upwind of JFJ could not explain the
182 measured concentrations of ice, while the addition of a surface flux of hoar crystals provided
183 the best agreement with observations. Although surface-originated processes have been
184 frequently invoked to explain the disparity between ICNCs and INPs, the role of SIP processes
185 – especially the BR and the DS mechanism – has received much less attention. In this study
186 we utilize the Weather Research and Forecasting model (WRF) to conduct simulations of two
187 case studies observed in winter during the CLACE 2014 campaign. Our primary objective is
188 to investigate if the implementation of two SIP parameterizations that account for the effect of
189 BR and DS can reduce the discrepancies between observed and simulated ICNCs. Additionally,
190 we aim to identify the conditions favoring the initiation of SIP in the orographic terrain and
191 explore the synergistic influence of SIP with wind-blown ice.

192

193 **2. Methods**

194 2.1 CLACE instrumentation

195 CLACE is a long-established series of campaigns taking place for over two decades at the
196 mountain-top station of JFJ, located in the Bernese Alps, in Switzerland, at an altitude of ~ 3580
197 m above sea level (a.s.l.) (e.g., Choularton et al., 2008). The measurement area is very complex
198 and heterogeneous with distinct mountain peaks (Fig. 1), while JFJ is covered by clouds
199 approximately 40% of the time, offering an ideal location for microphysical observations
200 (Baltensperger et al., 1998). Owing to the local orography surrounding the site, the wind flow
201 is constrained to two directions (Ketterer et al., 2014). Under southeasterly (SE) wind
202 conditions, air masses are lifted along the moderate slope of the Aletsch Glacier, whereas under
203 northwesterly (NW) wind conditions the air is forced to rise faster along the steep north face
204 of the Alps, which is associated with persistent MPCs (Lohmann et al., 2016). A detailed
205 description of the in-situ and remote sensing measurements taken during January and February



206 2014 as part of the CLACE 2014 campaign is provided by Lloyd et al. (2015) and Grazioli et
207 al. (2015). Here we only offer a brief presentation of the datasets used in this study.

208 Shadowgraphs of cloud particles were produced by the two-dimensional stereo
209 hydrometeor spectrometer (2D-S; Lawson et al., 2006), part of a three-view cloud particle
210 imager (3V-CPI) instrument. The 2D-S products have been used to provide information on the
211 number concentration and size distribution of particles in the size range of 10-1280 μm .
212 Following Crosier et al. (2011), the raw data were further processed to determine between ice
213 crystals and droplets, and to remove artefacts from shattering events (Korolev et al., 2011). An
214 approximation of the ice water content (IWC) at JFJ could also be derived by the 2D-S data
215 using the Brown and Francis (1995) mass-diameter relationship with a factor of up to 5
216 uncertainty (Heymsfield et al., 2010). Additionally, the quantification of the liquid water
217 content (LWC) is based on the liquid droplet size distribution data derived from a DMT cloud
218 droplet probe (CDP; Lance et al., 2010) over the size range between 2 and 50 μm . Typical
219 meteorological parameters (e.g., temperature, relative humidity, wind speed and wind
220 direction), that served as comparison to assess the validity of the model, were provided by the
221 weather station managed by MeteoSwiss at JFJ. The instrumentation was set up on the roof
222 terrace outside the Sphinx laboratory.

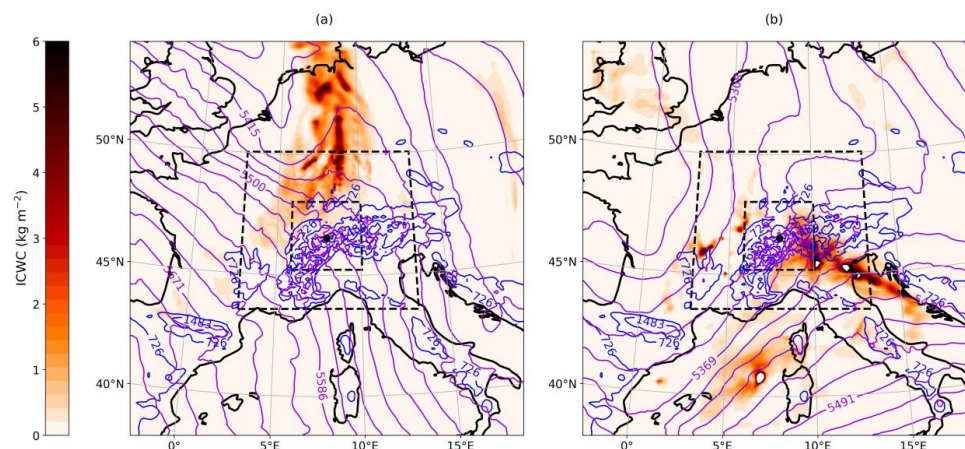
223

224 2.2 WRF simulations

225 WRF model, version 4.0.1, with augmented cloud microphysics (Sotiropoulou et al., 2021a) is
226 used for non-hydrostatic cloud-resolving simulations. The model has been run with three two-
227 way nested domains (Fig. 1), with a respective horizontal resolution of 12, 3 and 1 km. Two-
228 way grid nesting is generally found to improve the model performance in the inner domain
229 (e.g., Harris and Durran, 2010), although the sensitivity of the results to the applied nesting
230 technique has been shown to be negligible (not shown). The parent domain consists of 148 \times 148
231 grid points centered over the JFJ station (46.55 $^{\circ}$ N, 7.98 $^{\circ}$ E, shown with a black dot in Fig. 1),
232 while the second and the third domain include 241 \times 241 and 304 \times 304 grids, respectively. The
233 Lambert conformal projection is applied to all three domains, as it is well-suited for mid-
234 latitudes. Here we adapted the so-called “refined” vertical grid spacing proposed by Vignon et
235 al. (2021), using 100 vertical eta levels up to a model top of 50 hPa (i.e., \sim 20 km). This set-up
236 provides a refined vertical resolution of \sim 100 m up to mid-troposphere at the expense of the
237 coarsely resolved stratosphere. To investigate the dynamical influence on the development of
238 MPCs under the two distinct wind regimes prevailing at JFJ (Section 2.1), we simulate two



239 case studies, starting on 25 January and 29 January 2014, 00:00 UTC, respectively. Both case
240 studies are associated with the passage of frontal systems over the region of interest,
241 approaching the alpine slopes either from the NW (cold front) or the SE (warm front) direction,
242 as shown by the vertically-integrated condensed water content (ICWC; sum of cloud droplets,
243 rain, cloud ice, snow, and graupel) in Fig. 1. For both cases the simulation covers a 3-day
244 period, with the first 24 hours being considered sufficient time for spin up. A 27-s time step
245 was used in the parent domain and goes down to 9 s in the second domain and 3 s in the third
246 domain. Note that achieving such small time steps in the innermost domain is essential to
247 ensure numerical stability in non-hydrostatic simulations over a region with complex
248 orography such as around JFJ.
249



250
251 **Figure 1.** Map of synoptic conditions around JFJ station at (a) 00:00 UTC, 26 January 2014
252 and (b) 00:00 UTC, 30 January 2014, from the control simulation (12-km resolution domain).
253 The purple (blue) contours show the 500 hPa geopotential height in m (the terrain heights in
254 m). The color shading shows the vertically-integrated condensed water content (in kg m^{-2}). The
255 black dashed lines delimit the 3-km and 1-km resolution domains, while the black dot locates
256 the JFJ station.

257

258 The ERA5 reanalysis dataset (Hersbach et al., 2020) is used to initialize the model and
259 provide the lateral forcing at the edge of the 12-km resolution domain every 6 hours. Static
260 fields at each model grid point come from default WRF pre-processing system datasets, with a
261 resolution of 30" for both the topography and the 'land use' fields. The MODIS-based dataset
262 is used for land cover. Regarding the physics options chosen to run WRF simulations, the Rapid
263 Radiative Transfer Model for general circulation models (RRTMG) radiation scheme is applied
264 to parameterize both the short-wave and long-wave radiative transfer. The vertical turbulent



265 mixing is treated with the Mellor-Yamada-Janjic (MYJ; Janjić, 2002) 1.5 order scheme, while
266 surface options are modeled by the Noah land-surface model (Noah LSM; Chen and Dudhia,
267 2001). The Kain-Fritsch cumulus parameterization has been activated only in the outermost
268 domain, as the resolution of the two nested domains is sufficient to reasonably resolve cumulus-
269 type clouds at grid-scale.

270

271 *2.2.1 Microphysics scheme and primary ice production*

272 The Morrison two-moment scheme (Morrison et al., 2005; hereafter M05) is used to
273 parameterize the cloud microphysics, following the alpine cloud study of Farrington et al.
274 (2016). The scheme includes double-moment representations of rain, cloud ice, snow and
275 graupel species, while cloud droplets are treated with a single-moment approach and therefore
276 the droplet number concentration (N_d) must be prescribed. Here N_d is set to 100 cm^{-3} , based on
277 the mean N_d observed within the simulated temperature range (Lloyd et al., 2015).

278 Three primary ice production mechanisms through heterogeneous nucleation are
279 described in the default version of the M05 scheme, namely immersion freezing, contact
280 freezing, and deposition/condensation freezing nucleation. Immersion freezing of cloud
281 droplets and raindrops is described by the probabilistic approach of Bigg (1953). Contact
282 freezing is parameterized following Meyers et al. (1992). Finally, deposition and condensation
283 freezing is represented by the temperature-dependent equation derived by Rasmussen et al.
284 (2002) based on the in-situ measurements of Cooper (1986) collected from different locations
285 at different temperatures. Following Thompson et al. (2004), this parameterization is activated
286 either when there is saturation with respect to liquid water and the simulated temperatures are
287 below $-8 \text{ }^\circ\text{C}$ or when the saturation ratio with respect to ice exceeds a value of 1.08. The
288 accuracy of these parameterizations in representing atmospheric INPs is debatable as they are
289 derived from very localized measurements over a limited temperature range. Nevertheless,
290 Farrington et al. (2016) argued that the deposition/ condensation freezing parameterization of
291 Cooper (1986) can effectively explain INPs between the range 0.01 and 10 L^{-1} , which is
292 frequently observed during field campaigns at JFJ (Chou et al., 2011; Conen et al., 2015).

293

294 *2.2.2 Ice multiplication through rime splintering in the M05 scheme*

295 Apart from primary ice production, the HM process is the only SIP mechanism included in the
296 default version of the M05 scheme. This parameterization adapted from Reisner et al. (1998),
297 based on the laboratory findings of Hallett and Mossop (1974), allows for splinter production



298 after cloud- or rain- drops are collected by rimed snow particles or graupels. The efficiency of
299 this process is zero outside the temperature range between -8 and -3 °C, while it follows a
300 linear temperature-dependent relationship in between. HM is not activated unless the rimed ice
301 particles have masses larger than 0.1 g kg^{-1} and cloud or rain mass mixing ratio exceeds the
302 value of 0.5 g kg^{-1} or 0.1 g kg^{-1} , respectively. Since these conditions are rarely met in natural
303 MPCs, previous modeling studies had to artificially remove any thresholds to achieve an
304 enhanced efficiency of this process (Young et al., 2019; Atlas et al., 2020). In the current study,
305 however, the HM process is not effective, as the simulated temperatures at JFJ altitude are
306 below -8 °C (see Sect. 2.3).

307

308 2.2.3 Ice multiplication through ice-ice collisions in the M05 scheme

309 In addition to the HM process, we have also included two parameterizations to represent the
310 BR mechanism. An extensive description of the implementation method is provided in
311 Sotiropoulou et al. (2021a) (see their Appendix B). Among the three ice particle types included
312 in the M05 scheme (i.e., cloud ice, snow, graupel), we assume that only the collisions between
313 cloud ice-snow, cloud ice-graupel, graupel-snow, snow-snow, and graupel-graupel can result
314 in ice multiplication. The first parameterization tested here follows the simplified methodology
315 proposed by Sullivan et al. (2018a), which is based on the laboratory work of Takahashi et al.
316 (1995). Their findings revealed a strong temperature dependence of the fragment numbers
317 generated per collision (N_{BR}):

$$N_{BR} = 280 (T - T_{min})^{1.2} e^{-(T - T_{min})/5}, \quad (1)$$

318 where $T_{min} = 252 \text{ K}$, is the minimum temperature for which BR occurs. Yet their experimental
319 set-up was rather simplified involving only collisions between large hail-sized ice spheres with
320 diameters of ~ 2 cm. Taking this into account, Sotiropoulou et al. (2021a) further scaled the
321 temperature-dependent formulation for size:

$$N_{BR} = 280 (T - T_{min})^{1.2} e^{-(T - T_{min})/5} \frac{D}{D_0}, \quad (2)$$

322 where D is the size in meters of the particle that undergoes break-up and $D_0 = 0.02 \text{ m}$ is the size
323 of the hail-sized balls used in the experiments of Takahashi et al. (1995).

324 Phillips et al. (2017a) proposed a more physically-based formulation, developing an
325 energy-based interpretation of the experimental results conducted by Vardiman (1978) and
326 Takahashi et al. (1995). The initial collisional kinetic energy is considered as the governing
327 constraint driving the BR process. Moreover, the predicted N_{BR} depends on the ice particle type



328 and morphological habit and is a function of the temperature, particle size and rimed fraction.
329 Here the generated fragments per collision are described as follows:

$$N_{BR} = aA \left(1 - \exp \left\{ - \left[\frac{CK_0}{aA} \right]^\gamma \right\} \right), \quad (3)$$

330 where $K_0 = \frac{1}{2} \frac{m_1 m_2}{m_1 + m_2} (\Delta u_{n12})^2$ is the initial kinetic energy, in which m_1 and m_2 are the masses
331 of the colliding particles and $|\Delta u_{n12}| = \{(1.7 u_{n1} - u_{n2})^2 + 0.3 u_{n1} u_{n2}\}^{1/2}$ is the difference
332 in their terminal velocities. The correction term is proposed by Mizuno et al. (1990) and Reisner
333 et al. (1998) to account for underestimates when $u_{n1} \approx u_{n2}$. The parameter a in Eq. 3 is the
334 surface area of the smaller ice particle (or the one with the lower density), defined as $a = \pi D^2$,
335 with D as in Eq. 2. A in Eq. 3 represents the number density of breakable asperities on the
336 colliding surfaces. For collisions that involve cloud ice and snow particles A is described as
337 $A = 1.58 \times 10^7 (1 + 100\Psi^2) \left(1 + \frac{1.33 \times 10^{-4}}{D^{1.5}} \right)$, where $\Psi < 0.5$ is the rimed fraction of the most
338 fragile ice particle. For graupel-graupel collisions A is given by a temperature-dependent
339 equation as $A = \frac{a_0}{3} + \max \left(\frac{2a_0}{3} - \frac{a_0}{9} |T - 258|, 0 \right)$, in which $a_0 = 3.78 \times 10^4 \left(1 + \frac{0.0079}{D^{1.5}} \right)$. C
340 is the asperity-fragility coefficient, which is empirically derived to account for different
341 collision types, while the exponent γ is equal to 0.3 for collisions between graupel-graupel and
342 is calculated as a function of the rimed fraction for collisions including cloud ice and snow.
343 The parameterization was developed based on particles with diameters $500 \mu\text{m} < D < 5 \text{ mm}$,
344 however Phillips et al. (2017a) suggest that it can be used for particle sizes outside the
345 recommended range as long as the input variables to the scheme are set to the nearest limit of
346 the range. Finally, since N_{BR} was never observed to exceed 100 in the experiments of Vardiman
347 (1978), here we also use this value as an upper limit for all collision types (Phillips et al.,
348 2017a). All predicted fragments emitted through BR are added to the cloud ice category.
349

350 2.2.4 Ice multiplication through droplet shattering in the M05 scheme

351 Two different parameterizations are implemented in the M05 scheme to investigate the
352 potential efficiency of the DS mechanism in producing secondary ice splinters (N_{DS}). Phillips
353 et al. (2018) proposed two possible modes of raindrop-ice collisions, that can initiate the
354 freezing process. In the first mode, the freezing of the drop occurs either by collecting a small
355 ice particle or through heterogeneous freezing. In the default M05 scheme, the product of the
356 collisions between raindrops and cloud ice is considered to be graupel (snow) – if the rain
357 mixing ratio is greater (lower) than 0.1 g kg^{-1} , following Reisner et al. (1998). Additionally,



358 the heterogeneous freezing of big raindrops in the immersion mode follows Bigg's (1953)
359 parameterization (Section 2.2.1). Here we consider that the product of these two processes can
360 undergo shattering and generate numerous ice fragments, the number of which is parameterized
361 after Phillips et al. (2018). The formulation is derived by fitting to a pooled dataset from
362 laboratory studies and is given as a Lorentzian function of temperature and a polynomial
363 expression of the drop size. More precisely, in the first mode of the formulation, the total
364 number of fragments (N) generated per frozen drop are given by:

$$N = \mathcal{E}(D_r)\Omega(T) \left[\frac{\zeta\eta^2}{(T-T_0)^2 + \eta^2} + \beta T \right], \quad (4)$$

365 where T is the temperature (in K) and D_r is the size of the freezing raindrop (in mm). Note that
366 N is defined as the sum of the big fragments (N_B) and tiny splinters (N_T). Equation (4) applies
367 only to drop diameters less than 1.6 mm, which is the maximum observed experimentally. For
368 droplet sizes beyond this maximum value, N can be inferred by linear extrapolation. N_B is
369 described by another Lorentzian:

$$N_B = \min \left\{ \mathcal{E}(D_r)\Omega(T) \left[\frac{\zeta_B\eta_B^2}{(T-T_{B,0})^2 + \eta_B^2} \right], N \right\}. \quad (5)$$

370 The factors $\mathcal{E}(D_r)$ and $\Omega(T)$ in Eq. (4) and (5) are cubic interpolation functions, preventing the
371 onset of DS for $D_r < 0.05$ mm and $T > -3$ °C. Furthermore, the parameters ζ , η , T_0 , β , ζ_B , η_B ,
372 $T_{B,0}$, found in these relationships, are derived from previous laboratory studies and are
373 analytically described in Phillips et al. (2018). Note that the big fragments emitted (i.e., N_B)
374 will be initiated in the model as graupel, snow or frozen drops, while it is only the tiny splinters
375 ($N_T = N - N_B$) that are considered secondary ice (i.e., $N_{DS} = N_T$) and will be passed to the cloud
376 ice category.

377 The second mode of raindrop-ice collisions includes the accretion of raindrops on impact
378 with more massive ice particles, such as snow or graupel, the description of which in the M05
379 scheme is adapted from Ikawa and Saito (1991). This mode has been studied only once in the
380 laboratory study of Latham and Warwicker (1980), who reported that the collision of
381 supercooled raindrops with hailstones can potentially stimulate secondary ice. Since there was
382 no quantitative observation of this mode, Phillips et al. (2018) proposed an empirical, energy-
383 based formulation to account for the tiny splinters ejected after collisions between raindrops
384 and large ice particles:

$$N_{DS} = 3\Phi(T) \times [1 - f(T)] \times \max(DE - DE_{crit}, 0), \quad (6)$$



385 where $DE = \frac{K_0}{S_e}$, is the dimensionless energy given as the ratio of the initial kinetic energy (K_0 ;
386 described in 2.2.3) over the surface energy, which is expressed by the product $S_e = \gamma_{liq}\pi D_r^2$,
387 in which $\gamma_{liq}=0.073 \text{ J m}^{-2}$, is the surface tension of liquid water. The critical value of DE used
388 in Eq. (6) for the onset of splashing upon impact is set to $DE_{crit} = 0.2$. The parameter $f(T) =$
389 $-c_w T/L_f$, represents the initial frozen fraction of a supercooled drop during the first stage of
390 the freezing process, where $C_w = 4200 \text{ J kg}^{-1} \text{ K}^{-1}$, is the specific heat capacity of liquid water,
391 $L_f = 3.3 \times 10^5 \text{ J kg}^{-1}$, is the specific latent heat of freezing, while T is the initial freezing
392 temperature ($^{\circ}\text{C}$) of the raindrop. Finally, $\Phi(T) = \min[4f(T), 1]$ is an empirical fraction, which
393 represents the probability of any new drop in the splash products to contain a frost secondary
394 ice particle. At temperatures $\sim -10 \text{ }^{\circ}\text{C}$ this formulation yields $\Phi = 0.5$, meaning that the
395 probability of a secondary drop to contain ice is 50%. The first laboratory investigation of this
396 rather uncertain parameter as a function of temperature is provided in James et al. (2021).
397 Further details regarding the derivation of the empirical parameters and the uncertainties
398 underlying the mathematical formulations are discussed in Phillips et al. (2018).

399 Following Sullivan et al. (2018a), the second DS parameterization tested in this study is
400 described as the product of a polynomial expression of the freezing droplet size (Lawson et al.,
401 2015), a shattering probability (p_{sh}) and a freezing probability (p_{fr}):

$$N_{DS} = 2.5 \times 10^{-11} (D_r)^4 p_{sh} p_{fr} . \quad (7)$$

402 The p_{sh} is based upon droplet levitation experiments shown in Leisner et al. (2014) and is
403 represented by a temperature-dependent Gaussian distribution, centered at $\sim -15 \text{ }^{\circ}\text{C}$. Note that
404 p_{sh} is non-zero only for droplets with sizes greater than $50 \text{ }\mu\text{m}$. The p_{fr} is 0 for temperatures
405 warmer than $-3 \text{ }^{\circ}\text{C}$ and 1 if temperatures fall below $-6 \text{ }^{\circ}\text{C}$, following the cubic interpolation
406 function, $\Omega(T)$, adapted from Phillips et al. (2018).

407

408 2.3 Model validation

409 The control simulation (CNTRL), performed with the standard M05 scheme, sets the basis for
410 assessing the validity of the model against available meteorological observations. Temperature,
411 relative humidity, wind speed, and wind direction are obtained from the MeteoSwiss weather
412 station at JFJ. The comparison of each meteorological variable with the results from the nearest
413 model grid point of the CNTRL simulation is shown in Fig. 2. Note that the outputs are from
414 the first atmospheric level of the innermost domain at $\sim 10 \text{ m}$ above ground level (a.g.l) (Fig.
415 1), while the first 24 hours of each simulation period are considered spin up time and are

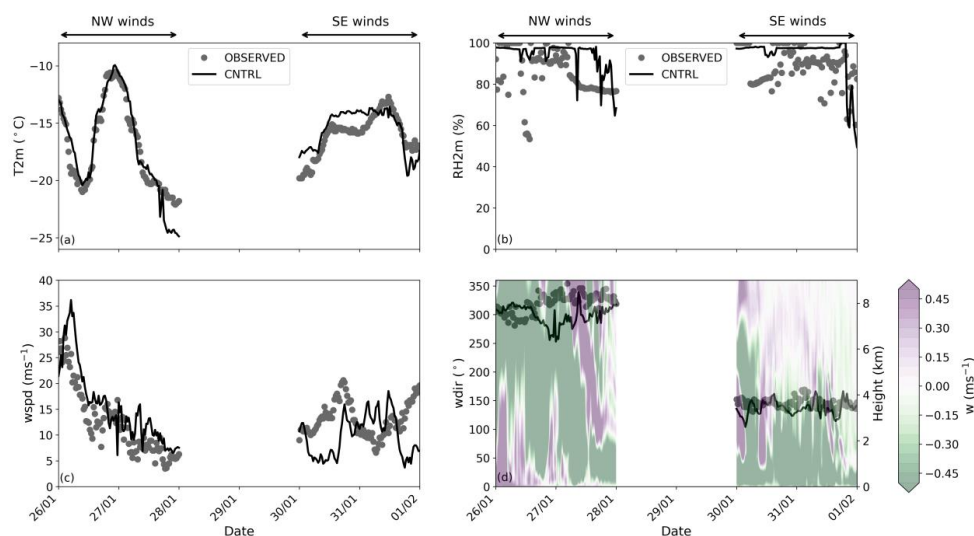


416 therefore excluded from the present analysis. The mean modeled values and standard
 417 deviations (std), along with the root mean square error (RMSE) and the index of agreement
 418 (IoA) between model predictions and observational data are summarized in Table 1. IoA is
 419 both a relative and a bounded measure (i.e., $0 \leq \text{IoA} \leq 1$) that describes phase errors between
 420 predicted (P_i) and observed (O_i) time series (Willmott et al., 2012):

$$\text{IoA} = 1 - \left[\frac{\sum_{i=1}^N (P_i - O_i)^2}{\sum_{i=1}^N (|P_i| + |O_i|)^2} \right], \quad (8)$$

421 where $P'_i = P_i - \bar{O}$ and $O'_i = O_i - \bar{O}$, in which \bar{O} is the mean of the observed variable.

422



423 **Figure 2.** Time series of (a) temperature (T_{2m}), (b) relative humidity with respect to liquid phase at 2m height (RH_{2m}), (c) wind speed ($wspd$) and (d) wind direction ($wdir$). Grey circles
 424 indicate measurements collected between 26 January and 1 February 2014 at JFJ station, while
 425 modeled values from CNTRL simulation are shown with a black line. The semi-transparent
 426 contour plot is representing the vertical velocity (w) profile predicted by the CNTRL
 427 simulation. Each day starts at 00:00 UTC.
 428
 429

430

431 Throughout the two case studies, the WRF simulations seem to closely follow the
 432 observed temperatures (Fig. 2a), which is also indicated by the high IoA in Table 1. The
 433 synoptic situation occurring on 26 January, with a deep trough extending to western Europe
 434 (Fig. 1), has been associated with intense snowfalls in the alpine regions (Panziera and Hoskins,
 435 2008). The passage of the cold front was followed by a sharp temperature decrease, with the
 436 simulated temperatures fluctuating between -10 and ~ -20 °C throughout the NW case (Fig.
 437 2a). Under the influence of the warm front during the SE case, the modeled temperatures rose



438 from ~ -18 °C to ~ -14 °C and remained less variable until 30 January 12:00 UTC, with mean
439 values of ~ -15.5 °C (Table 1).

440

441 **Table 1.** Mean modeled values (\pm standard deviations), RMSE and IoA between the CNTRL
442 simulation of WRF and measurements carried out by the MeteoSwiss station at JFJ.

Variable	Mean \pm std		RMSE		IoA	
	NW winds	SE winds	NW winds	SE winds	NW winds	SE winds
T2m (°C)	-17.10 ± 4.36	-15.48 ± 1.75	1.40	1.33	0.97	0.84
RH2m (%)	94.07 ± 7.02	94.24 ± 10.31	14.01	11.61	0.55	0.64
wspd (ms^{-1})	15.57 ± 7.45	9.78 ± 3.94	4.85	6.75	0.88	0.22

443

444 Fig. 2c and 2d reveal that the 1-km resolution domain can sufficiently capture the local
445 wind systems to a certain extent. During the NW flow, the horizontal wind speeds are
446 reproduced better by the CNTRL simulation (IoA=88%), whereas during the SE winds, the
447 simulated wind speed is frequently underestimated compared with observations (Fig. 2c). Such
448 deviations in the horizontal wind speed might be caused by the relatively coarse horizontal
449 resolution of the model, which prevents some small-scale and very local orographic structures
450 from being resolved. As discussed in Section 2.2, the observed winds at JFJ are channeled by
451 the orography to either NW or SE directions. The CNTRL simulation of WRF can satisfactorily
452 reproduce the wind direction in both cases, although the simulated values exhibit larger
453 fluctuations than the measured ones (Fig. 2d), presumably because of the surrounding
454 orography being less accurately represented in the model. This is particularly evident during
455 NW winds, when the simulated wind directions shift slightly to west directions compared to
456 observations. The positive vertical velocities, illustrated in the contour plot in Fig. 2d, result
457 from the orographically forced lifting of the airmasses over the local topography, and are not
458 related to convective instability in the lower atmospheric levels. The stronger updrafts
459 prevailing until the end of 26 January are associated with the steep ascent of the air parcels,
460 which can also contribute to the enhanced relative humidity (Fig. 2b). After the frontal passage,
461 the vertical velocities at the lower levels are downward directed, with the vertical profile of
462 potential temperature revealing that the atmosphere at JFJ is stabilized (not shown). The same
463 vertical velocity pattern, with mainly downward motions, characterizes the stably stratified



464 atmosphere after 30 January. Overall, Fig. 2 suggests that local meteorological conditions at
465 JFJ are reasonably well represented by the model.

466

467 2.4 Model simulations

468 Given the good representation of the atmospheric conditions at JFJ, the CNTRL simulation of
469 WRF is further accompanied by four sensitivity simulations, aiming to investigate the
470 contribution of BR and DS mechanisms. Here we also perform three additional sensitivity
471 experiments to explore the potential impact of blowing ice and the synergistic interaction with
472 SIP on the development of the simulated MPCs. A detailed list of the sensitivity experiments
473 is provided in Table 2.

474 The contribution of the DS mechanism is addressed in two sensitivity experiments,
475 DS_PHILL and DS_SULL, where the parameterizations of Phillips et al. (2018) and Sullivan
476 et al. (2018a) were applied, respectively (Section 2.2.4). Both sensitivity simulations yield
477 predictions that coincide with the CNTRL simulation (supplement Fig. S1) suggesting that the
478 DS mechanism is hardly ever activated, and fail to produce realistic total ice number
479 concentrations (N_{isg} ; cloud ice + snow + graupel). The absence of correlation between LWC
480 and N_{isg} fluctuations might also suggest the ineffectiveness of this mechanism under the
481 examined conditions. Note that the parameterized expressions used to describe the DS
482 mechanism involve a number of empirical and rather uncertain parameters, the value of which
483 could potentially influence the efficiency of the process in producing secondary ice fragments.
484 However, the sensitivity of our results to the choice of these parameters would be negligible,
485 as the low concentrations ($\lesssim 10\text{-}2\text{ cm}^{-3}$) of relatively small raindrops with mode diameters
486 below the threshold size of $50\text{ }\mu\text{m}$ seem to completely prevent the onset of the DS process
487 (supplement Fig. S2). The DS mechanism is therefore excluded from the following discussion.
488 This result is in line with the modeling study of Dedekind et al. (2021), who also highlighted
489 the inefficiency of this mechanism in wintertime alpine clouds.

490 Two additional sensitivity simulations are conducted to investigate if the BR mechanism
491 can account for the observed ICNCs. First, the temperature-dependent formula of Takahashi et
492 al. (1995) scaled with the size of the particles that undergo fragmentation (Sotiropoulou et al.
493 2021a) is tested in the TAKAH simulation. The PHILL simulation is then conducted to test the
494 performance of the more advanced Phillips et al. (2017a) parameterization. Note that the
495 parameters involved in the parameterized expression of N_{BR} (Eq. 3) concern the effect of ice
496 habit and rimed fraction of the colliding ice particles – which is not explicitly resolved in the



497 M05 scheme. Regarding the ice habit, we assume spatial planar ice particles, based on the
498 imagery presented in Lloyd et al. (2015) and Grazioli et al. (2015), which revealed the
499 predominance of sectored plates and oblate particles (probably columns or needles), along with
500 some rimed hydrometeors, at temperatures ~ -15 °C. Balloon-borne measurements taken in
501 low-level orographic MPCs within seeder-feeder events revealed the presence of a large
502 fraction of graupel and rimed particles (Ramelli et al., 2021). For this reason, during the NW
503 and SE cases we consider rimed fractions of 0.4 and 0.3 to account for heavily and moderately
504 rimed ice particles, respectively. A higher rimed fraction is prescribed for the NW-winds case
505 study though, as the co-existence of ice crystals and liquid droplets under the stronger updraft
506 conditions are expected to favor ice crystal growth through riming. However, the sensitivity of
507 our results to the rimed fraction was not found significant.

508

509 **Table 2.** List of sensitivity simulations conducted with the WRF model.

Simulation	BR process	DS process	NBIPS (L^{-1})
CNTRL	off	off	0
DS_PHILL	off	Phillips et al., 2018	0
DS_SULL	off	Sullivan et al., 2018a	0
TAKAH	Takahashi et al., 1995	off	0
PHILL	Phillips et al., 2017a	off	0
BIPS10	off	off	10
BIPS100	off	off	100
BIPS100_PHILL	Phillips et al., 2017a	off	100

510

511 The remaining sensitivity simulations focus on the potential impact of BIPS. Given that
512 in the default M05 scheme there is no parameterization of a flux of ice particles from the
513 surface, we parameterize the effect of BIPS lofting into the simulated orographic clouds by
514 applying a constant ice crystal source to the first atmospheric level of WRF over the whole
515 model domain. Although the source of BIPS at the first model level remained constant, yet
516 their number will be affected by processes such as advection, sublimation and sedimentation,
517 that are described in the M05 scheme. Note that the relatively coarse horizontal resolution in
518 the innermost domain of our simulations (i.e., 1 km) does not allow the accurate representation
519 of the small-scale turbulent flow over the orographic terrain. This is considered a limitation of
520 our methodology, since turbulent diffusion is a key process affecting the amount of BIPS that
521 will be resuspended from the surface.



522 The applied concentrations of BIPS varied between 10^{-2} and 100 L^{-1} , which is the upper
523 limit proposed by Lloyd et al. (2015) and observed within in-cloud conditions by Beck et al.
524 (2018). Number concentrations of BIPS (i.e., NBIPS) lower than 10 L^{-1} were found incapable
525 of affecting the simulated cloud properties and are, therefore, not included in the following
526 discussion. Two sensitivity simulations are finally performed, BIPS10 and BIPS100 (Table 2),
527 in which the number indicates the NBIPS in L^{-1} . In our approach we assume BIPS are spherical
528 with diameters of $100 \mu\text{m}$, based on typical sizes that are frequently reported in the literature
529 (e.g., Schlenczek et al., 2014; Schmidt, 1984; Geerts et al., 2015). The relatively small fall
530 speed of these particles (e.g., Pruppacher and Klett, 1997) will allow them to remain suspended
531 in the atmosphere. As a sensitivity we also considered smaller particles with sizes of $10 \mu\text{m}$,
532 but our results did not change significantly (supplement Fig. S3). Besides, such small ice
533 particles are not expected to substantially contribute to the simulated IWC, as shown by
534 Farrington et al. (2016).

535 As SIP through BR and blowing snow are both important when trying to explain the high
536 ICNCs observed in alpine environments, their combined effect is addressed in our last
537 simulation, BIPS100_PHILL (Table 2). In this sensitivity simulation the effect of BR is
538 parameterized after Phillips et al. (2017a), while a constant ice crystal concentration of 100 L^{-1}
539 is applied to the first atmospheric level of WRF to represent the effect of BIPS.

540

541 3. Results and discussion

542

543 3.1 Impact of SIP through BR on simulated microphysical properties

544 Fig. 3 displays the temporal evolution of the N_{isg} , IWC and LWC, at the first model level (~ 10
545 m a.g.l.) from the nearest to JFJ model grid point of the CNTRL, TAKAH and PHILL
546 simulations. Note that instead of focusing on a single grid point, we averaged the results from
547 the 9-km^2 area surrounding the point of interest. However, the produced time series showed
548 only little difference when compared to the nearest grid point time series, further validating the
549 robustness of our results (not shown). Besides, the region in the vicinity of JFJ is very
550 heterogeneous supporting the single point comparison presented in the following discussion.
551 The grey dots shown in Fig. 3 represent the measurements taken by the 2D-S and CDP
552 instruments at JFJ throughout the two periods of interest. The displayed time frequency of the
553 observations is 30 min to match the output frequency of the model. Note that the simulated
554 LWC includes liquid water from cloud droplets and rain, while the simulated IWC includes



555 cloud ice, snow and graupel. The contribution of rain in our simulations is, however, negligible
556 (supplement Fig. S2). Several statistical metrics for N_{isg} , IWC and LWC are summarized in
557 Table 3, 4 and 5, respectively. Note that periods with missing data in the measurement time
558 series are excluded from the statistical analysis.

559 During the NW flow, between 26 and 28 January, the measured ICNCs exceed 100 L^{-1}
560 for >50 % of the time, whereas during the SE flow the ICNCs usually fluctuate between 10 and
561 100 L^{-1} (Fig. 3a). The highest ICNCs are generally observed at temperatures higher than ~ -15
562 $^{\circ}\text{C}$, where SIP processes are thought to be dominant and primary ice nucleation in the absence
563 of bioaerosols is limited (e.g., Hoose and Möhler, 2012; Kanji et al., 2017). The CNTRL
564 simulation fails to reproduce N_{isg} higher than 10 L^{-1} , with the mean simulated values being ~ 2 -
565 2.5 L^{-1} during both periods. At the same time the mean observed ICNC values are ~ 200 (70)
566 L^{-1} during the NW (SE) case. Thus CNTRL systematically underestimates the amount of ice
567 by up to 2 orders of magnitude, which is also consistent with the interquartile statistics
568 presented in Table 3. With the HM process being totally ineffective in the prevailing
569 temperatures, this discrepancy suggests that ice crystals produced by heterogeneous ice
570 nucleation in CNTRL are not high enough to match the observations. A similar discrepancy
571 between predicted INPs and measured ICNCs was also documented in Lloyd et al. (2015).

572

573 **Table 3.** The 25th, 50th (median) and 75th percentiles of ICNC time series (in L^{-1}).

Simulation	25 th perc.		Median		75 th perc.	
	NW winds	SE winds	NW winds	SE winds	NW winds	SE winds
OBSERVED	8.69	6.64	80.47	34.53	261.25	88.69
CNTRL	0.76	0.84	1.68	2.02	2.80	3.60
TAKAH	2.27	1.08	9.85	122.56	362.51	358.38
PHILL	2.49	0.76	6.27	2.09	118.21	59.23
BIPS10	1.60	1.90	2.42	2.72	3.30	4.78
BIPS100	6.17	10.74	10.36	13.88	12.32	17.39
BIPS100_PHILL	8.95	11.51	15.87	16.30	138.92	98.43

574

575 Activating the BR process in TAKAH and PHILL simulations is found to produce N_{isg}
576 as high as 400 L^{-1} during both case studies (Fig. 3a), resulting in a substantially better
577 agreement with observations. At times when the simulated temperatures drop below $\sim -18 \text{ }^{\circ}\text{C}$,
578 the N_{isg} modeled by both simulations coincide with the CNTRL simulation. At relatively
579 warmer subzero temperatures though, the significant contribution of the BR process is evident,



580 elevating the predicted N_{isg} by up to 3 orders of magnitude during the NW case and by more
581 than 2 orders of magnitude during the SE case. Although the median N_{isg} in TAKAH and
582 PHILL remains underestimated compared to observations during the NW flow, the first seems
583 to produce unrealistically high median and 75th percentile values during the SE flow (Table 3).
584 Indeed, focusing on the N_{isg} time series (Fig. 3a) TAKAH is ~25% of the time shown to
585 overestimate the observed ICNCs by a factor of ~3, reaching up a factor of 10 on 30 January
586 at 00:00. PHILL, on the other hand, produces more reasonable N_{isg} throughout both case
587 studies, increasing N_{isg} in the 75th percentile by more than 100 (50) L⁻¹ during the NW (SE)
588 case study (Table 3), reducing the gap between observations and model predictions.
589

590 **Table 4.** The 25th, 50th (median) and 75th percentiles of IWC (in gm⁻³) time series.

Simulation	25 th perc.		Median		75 th perc.	
	NW winds	SE winds	NW winds	SE winds	NW winds	SE winds
OBSERVED	31.5×10^{-3}	22.0×10^{-3}	0.63	0.24	0.66	0.26
CNTRL	4.3×10^{-3}	5.0×10^{-3}	0.03	0.04	0.15	0.12
TAKAH	1.3×10^{-3}	2.0×10^{-3}	0.10	0.09	0.52	0.34
PHILL	3.8×10^{-3}	3.7×10^{-3}	0.10	0.02	0.38	0.30
BIPS100_PHILL	3.9×10^{-3}	9.0×10^{-3}	0.09	0.03	0.40	0.31

591

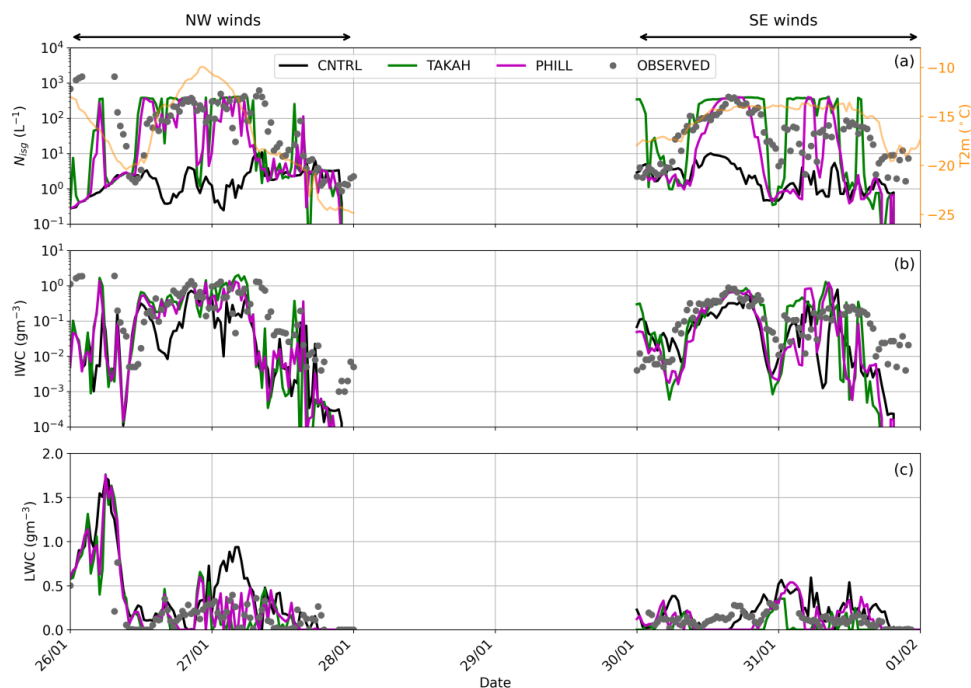
592 The observed IWC time series (Fig. 3b) are frequently reaching ~1 gm⁻³ during the NW
593 case, with the median values being a factor of 2.5 higher than those observed during the SE
594 case (Table 4). This highlights the presence of more massive ice particles when higher updraft
595 velocities prevail. The CNTRL simulation cannot produce IWC values > 0.8 gm⁻³ and is most
596 of the time below the observed range. Adding a description of the BR process in TAKAH and
597 PHILL simulations sufficiently increases the modeled IWC by up to ~1 order of magnitude
598 between 26 January 12:00 UTC and 27 January 06:00 UTC, when the modeled N_{isg} exceeds
599 100 L⁻¹ and the temperatures remain higher than -16 °C. The same conditions are observed in
600 the SE case, between 12:00 and 18:00 UTC on 30 January, when IWC shows a ~3 fold
601 enhancement reaching the observed levels. The IWC values in the third quartile predicted by
602 TAKAH and PHILL are more than a factor of 2 higher than the ones predicted by CNTRL
603 (Table 4). This increase improves the model performance although the modeled IWC remains
604 slightly underestimated (overestimated) during the NW (SE) case. The size distribution of the
605 three ice hydrometeors assumed by all three sensitivity simulations (supplement Fig. S4)
606 reveals that the implementation of the BR mechanism produces elevated concentrations of



607 cloud ice crystals but at the same time increases the concentrations of snow particles. This is
608 the reason why the modeled total ice mass is also increased compared with the CNTRL
609 simulation.

610 Fig. 3c compares the simulated cloud LWC to the concurrent CDP observations at JFJ
611 station. The LWC values recorded during the NW case are highly variant, reaching up to 0.75
612 gm^{-3} , which is substantially higher than the respective maximum LWC observed during the SE
613 case (0.30 gm^{-3}). On 26 January before 12:00 UTC, all three sensitivity simulations predict
614 $\text{LWC} > 1 \text{ gm}^{-3}$, which, however, cannot be validated against measurements due to missing
615 values in the CDP time series. Note that this period is excluded from the statistics derived in
616 Table 5. The CNTRL simulation is found to overestimate the cloud LWC, predicting 0.42
617 (0.25) gm^{-3} in the third quartile, which is a factor of ~ 2 higher than the mean LWC observed
618 during the NW (SE) case (Table 5).

619



620
621 **Figure 3.** Time series of (a) total N_{isg} and temperature at 2 m height (orange line), (b) IWC and
622 (c) LWC, predicted by the CNTRL (black line), TAKAH (green line) and PHILL (magenta line) simulations between 26 January and 1 February 2014. The grey dots in all three panels
623 represent the 2D-S ICNCs, the inferred IWC and the CDP LWC measured at the JFJ station,
624 respectively. Note the logarithmic y-axes in panels a and b.
625

626



627 The modeled LWC in the 75th percentile is decreased by a factor of >2.5 (~1.5) in
628 TAKAH (PHILL) simulations (Table 5), improving the agreement with observations (Fig. 3c).
629 This reduction in LWC is expected, considering that the higher N_{isg} produced when BR is
630 activated can readily deplete the surrounding droplets under liquid water subsaturated
631 conditions through the WBF process. This introduces a challenging environment to simulate,
632 as the model is sometimes seen to convert water to ice too rapidly, leading to cloud glaciation
633 (e.g., on 30 January after 12:00 UTC). Despite all sinks of cloud water (i.e., condensation
634 freezing, WBF or riming), observations at JFJ suggest that mixed-phase regions are generally
635 sustained (Lloyd et al., 2015). This is particularly true for the NW case, when the sufficiently
636 large updrafts caused by the steep ascent of the air masses help maintain the supersaturation
637 with respect to liquid water (Lohmann et al., 2016). PHILL can more efficiently sustain the
638 observed mixed-phase conditions compared to TAKAH, which frequently results in explosive
639 ice multiplication – especially during the SE case – leading to an underestimation of the LWC
640 (see Fig. 3c and Table 5).

641

642 **Table 5.** The 25th, 50th (median) and 75th percentiles of LWC (in gm^{-3}) time series.

Simulation	25 th perc.		Median		75 th perc.	
	NW winds	SE winds	NW winds	SE winds	NW winds	SE winds
OBSERVED	8.5×10^{-3}	70.0×10^{-3}	0.12	0.11	0.21	0.14
CNTRL	87.7×10^{-3}	26.0×10^{-3}	0.19	0.17	0.42	0.25
TAKAH	1.3×10^{-10}	0.0	0.01	6.7×10^{-10}	0.16	0.05
PHILL	6.3×10^{-8}	0.0	0.09	0.03	0.26	0.18
BIPS10	82.0×10^{-3}	4.6×10^{-3}	0.18	0.12	0.33	0.24
BIPS100	67.1×10^{-3}	13.1×10^{-3}	0.18	0.13	0.36	0.23
BIPS100_PHILL	6.3×10^{-10}	0.0	0.09	0.06	0.27	0.10

643

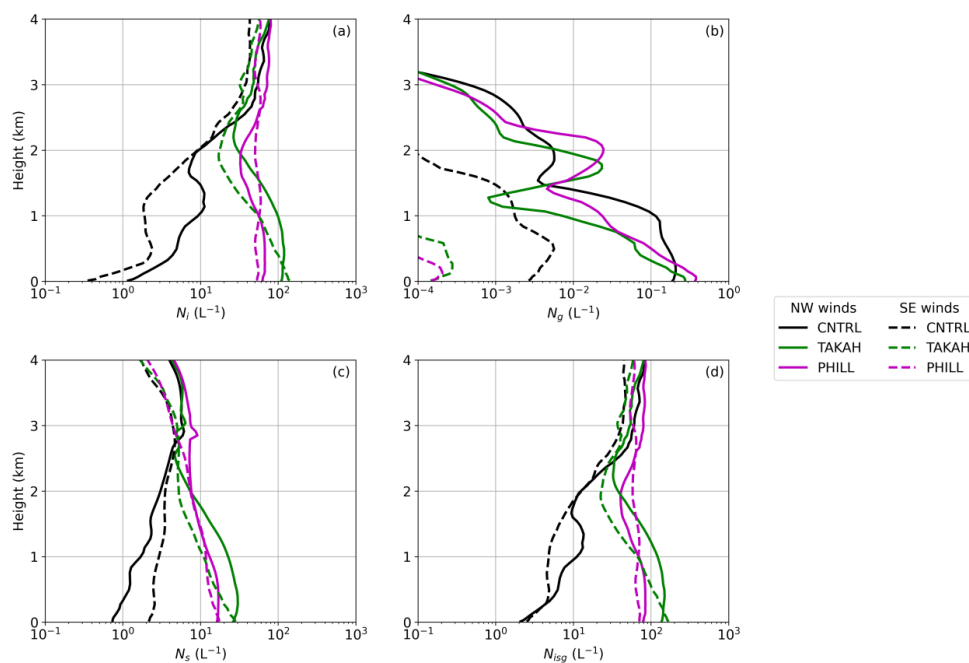
644 The time-averaged vertical profiles of number concentrations of cloud ice (N_i), graupel
645 (N_g), snow (N_s) and total N_{isg} are illustrated in Fig. 4 for the CNTRL, TAKAH and PHILL
646 simulations. N_i (Fig. 4a) and N_{isg} (Fig. 4d) are enhanced by more than 2 orders of magnitude in
647 TAKAH and PHILL compared to CNTRL. It is again obvious that TAKAH produces higher
648 concentrations than PHILL, at least in the lower 2 (1) km of the atmosphere during the NW
649 (SE) case. As discussed above, this regularly leads to overestimated N_{isg} compared with the
650 observed amount of ice close to the surface. All three simulations, however, produce similar
651 results at heights above ~2.5 km, where the simulated temperatures drop well below -20°C



652 (supplement Fig. S5). This implies the greater importance of SIP through BR at heights below
653 2-3 km in the atmosphere (i.e., in the temperature range between ~ -18 °C and ~ -10 °C).

654 Graupel number concentrations (Fig. 4b) do not contribute much to the modeled ice
655 phase, especially during the SE case when the simulated N_g is negligible compared with the N_i
656 and N_s (Fig. 4c). In the M05 scheme, portion of the rimed cloud or rain water onto snow is
657 allowed to convert into graupel (Reisner et al. 1998), provided that snow, cloud liquid and rain
658 water mixing ratios exceed a threshold of 0.1, 0.5 and 0.1 g kg^{-1} , respectively. These mixing
659 ratio thresholds for graupel formation are arbitrary and might not be suitable for the examined
660 conditions, preventing the formation of graupel from rimed snowflakes (Morrison and
661 Grabowski, 2008). During the NW case, however, we can identify substantially higher N_g than
662 the SE case, owing to the presence of sufficient supercooled liquid water especially during the
663 first half of 26 January. Activating the BR mechanism in TAKAH and PHILL generally
664 decreases the simulated N_g in both cases (Fig. 4c), suggesting that break-up of graupel
665 contributes to ice multiplication.

666



667

668 **Figure 4.** Mean vertical profiles of (a) N_i , (b) N_g , (c) N_s and (d) total N_{isg} , predicted by the
669 CNTRL (black), TAKAH (green) and PHILL (magenta) simulations for the NW (solid lines)
670 and SE (dashed lines) cases. Note the different scale on the x axis of the N_g vertical distribution.
671 The height is given in km a.g.l.



672

673 The mean vertical profile of N_s (Fig. 4c) seems to follow the respective profile of N_i (Fig.
674 4a). Unlike the graupel concentrations, including the BR mechanism is found to enhance N_s up
675 to one order of magnitude compared to the CNTRL simulation. Focusing on a single model
676 time step when the BR mechanism is activated, the size distribution of snow particles shown
677 in the supplement Fig. S4 reveals that the increase in snow number concentrations can reach
678 up to 2 orders of magnitude during the NW case. This is a logical consequence of the increase
679 in number concentration of ice crystals, which are converting to snow particles after ice crystal
680 growth (i.e., cloud-ice-to-snow autoconversion), when surpassing a characteristic mean
681 diameter of 250 μm . This will be discussed in detail in the following section, which is focused
682 on PHILL simulation as it provides a slightly more accurate representation of the in-cloud
683 phase partitioning compared with TAKAH.

684

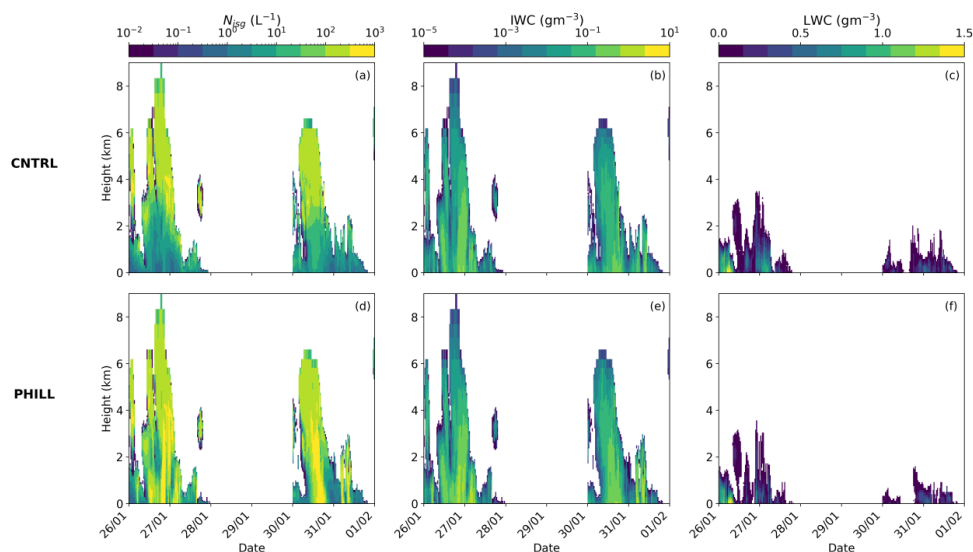
685 3.1.1 Conditions favoring BR in the two considered events

686 The temporal evolution of the vertical profiles of N_{isg} , IWC and LWC can provide valuable
687 insight on the drivers of enhanced ice formation in the wintertime alpine MPCs. Fig. 5 reveals
688 the presence of a seeder-feeder cloud system with sustained mixed-phase conditions confined
689 to levels below ~ 3 km (~ 1.5 km) in the NW (SE) case and a pure ice cloud aloft. Such
690 configurations are a well-known type of orographic multi-layer clouds that enhances
691 precipitation over mountains (e.g., Browning et al., 1974, 1975; Roe, 2005). Cloud
692 condensation is promoted by the synergy between a midlatitude frontal system and its
693 orographically induced ascent over the mountain range (Fig. 1). The separation between the
694 seeder and feeder clouds is often nonexistent, meaning that ice seeding can occur either in
695 layered clouds or internally within one cloud (Roe, 2005; Proske et al., 2021). In the first case,
696 which seems to occur here as well, there can be vertical continuum of cloud condensates
697 between the seeder and the feeder cloud due to precipitation of ice crystals from the higher-
698 level cloud (Fig. 5a). This means that the seeding ice crystals fall through subsaturated cloud-
699 free air before reaching the feeder region of the cloud and might sublimate. A remote-sensing
700 analysis to 11-year of data over Switzerland showed that in-cloud seeding occurs in 18% of the
701 observations, while the external seeder-feeder mechanism is present 15% of the time (Proske
702 et al., 2021) when the seeder is a cirrus cloud.

703 To illustrate the processes taking place during the two cases of interest, Fig. 6 displays
704 the tendency of primary and secondary ice production as well as the growth of ice particles



705 through deposition, riming and aggregation from the CNTRL and PHILL simulations at 17:00
706 (19:00) UTC on 26 (30) January. The vertical profiles on 26 January are taken within the
707 seeder-feeder event, while those on 30 January are taken when the high-level cloud associated
708 with the warm front has already passed the region of interest. Upon arrival of the frontal system
709 on 26 January, the CNTRL simulation indicates a rapid increase of the total N_{isg} near cloud top
710 (Fig. 5a), which is not shown in the vertical profile of the primary ice production rates taken at
711 17:00 UTC (Fig. 6a). The ice particles consisting the seeder cloud are, therefore, formed far
712 from the JFJ station and seem to be advected over the domain of interest. Primary ice crystals
713 are formed in both cases below 2 km in the feeder cloud at temperatures lower than -30 °C
714 through heterogeneous freezing (Fig. 6a). At these heights supercooled liquid water is also
715 present (Fig. 5c) and the newly formed ice particles start growing initially by vapor deposition
716 due to supersaturation with respect to ice, followed by riming (Fig. 6b). This is also indicated
717 by the increased IWC values closer to the ground (Fig. 5b).
718



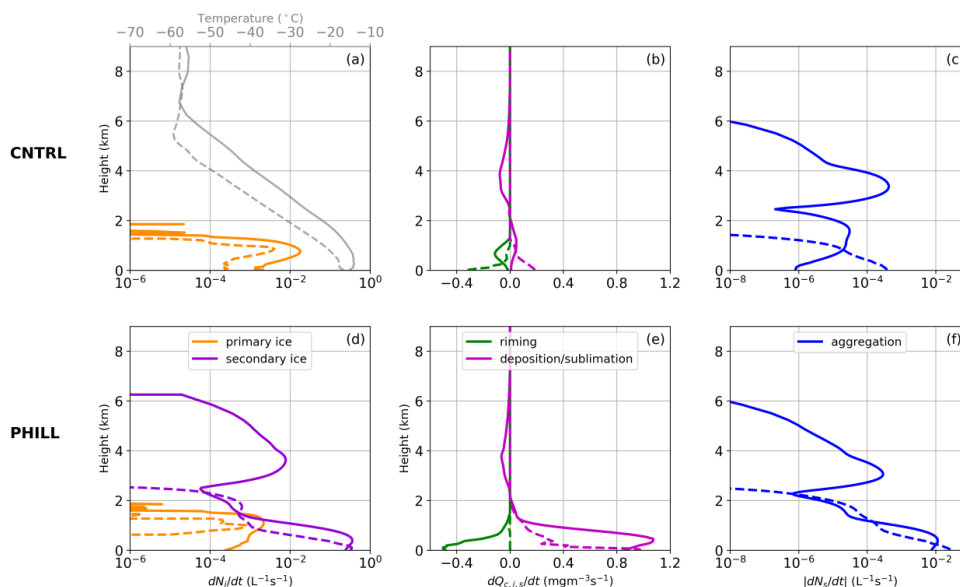
719
720 **Figure 5.** Time-height plots of total N_{isg} (a, d), IWC (b, e) and LWC (c, f) produced by CNTRL
721 (top panel) and PHILL (bottom panel) simulations between 26 January and 1 February 2014.
722 The height is given in km a.g.l.

723

724 Focusing on the ice-seeding event of 26 January, the enhanced aggregation rate observed
725 at heights above ~ 2.5 km in the atmosphere indicates the enhanced collision efficiencies of the
726 precipitating ice particles while falling from the seeder cloud (Fig. 6c). Note that a portion of
727 the sedimented ice particles sublimates before reaching the feeder cloud at heights ~ 3 -5 km,



728 indicating the prevailing unsaturated conditions in this layer (Fig. 6b). Within this layer the
729 aggregation of snowflakes weakens, while it is enhanced again when the falling hydrometeors
730 enter the feeder cloud. The bottom line is that, even under the simulated seeder-feeder events
731 the concentrations of ice particles reaching the ground in CNTRL simulation remain severely
732 underestimated (Section 3.1). Despite the low concentrations of ice crystals simulated by the
733 CNTRL simulation, the low-level cloud is glaciated more frequently during the SE than during
734 the NW winds case (Fig. 5c). This is probably because of the higher updraft velocities
735 prevailing until 28 January (Fig. 2d), preventing ice crystals from falling through the lower
736 parts of the cloud (Lohmann et al., 2016).
737



738
739 **Figure 6.** Vertical profiles of (a, d) primary and secondary ice production, (b, e) riming and
740 vapor deposition or sublimation and (c, f) snow aggregation produced by the CNTRL (top
741 panel) and PHILL (bottom panel) simulations at 17:00 UTC on 26 January (solid line) and at
742 19:00 UTC on 30 January (dashed line). The vertical profile of simulated temperature is also
743 superimposed in (a). The cloud liquid water content (Q_c) is shown in panels (b and e) to
744 represent the tendency due to riming, while the mass mixing ratio of the ice and snow species
745 ($Q_i + Q_s$), are representing the relative tendencies due to vapor deposition or sublimation. Note
746 that the tendencies due to snow aggregation in (c, f) are presented in absolute values. The height
747 is given in km a.g.l.

748 Activating the BR mechanism along with the seeding of precipitating hydrometeors in
749 PHILL simulation shifts the simulated N_{isg} towards higher concentrations that are found to
750 exceed 300 L⁻¹ in the lower-level part of the cloud (Fig. 5d). On 26 January the mode of the
751 cloud ice distribution shifts to slightly bigger sizes, while on 30 January the modal sizes



752 become almost an order of magnitude smaller compared with the CNTRL simulation
753 (supplement Fig. S4). The enhanced concentrations of bigger ice particles simulated in the first
754 case experience rapid growth through vapor deposition and riming (Fig. 6e) causing a slight
755 increase in the simulated IWC (Fig. 5e) at the expense of the surrounding cloud droplets in the
756 low-level feeder cloud (Fig. 5f). Nevertheless, the smaller ice particles simulated in the second
757 case grow less efficiently through vapor deposition, while the explosive multiplication of ice
758 through BR seems to fully glaciare the low-level cloud below ~1 km resulting in an almost zero
759 riming rate (Fig. 6e). The reduced primary ice production rate observed during both case
760 studies is a consequence of the depletion of liquid water when BR is considered (Fig. 6d).

761 The key difference between CNTRL and PHILL simulations is that the latter takes
762 advantage of the enhanced ice particle growth through aggregation while falling to the feeder
763 cloud below ~2 km, where large snowflakes coexist with smaller ice crystals (Fig. 4a, 6a, 6d).
764 This allows for differential settling, which enhances collision efficiency facilitating ice
765 multiplication through BR. This is the reason why the vertical profile of secondary ice
766 formation agrees with the corresponding profile of aggregation during both case studies (Fig.
767 6d, 6f). On 26 January the first secondary ice particles start forming already within the seeder
768 cloud with the contribution of SIP increasing considerably when reaching the feeder cloud,
769 where the tendency due to SIP is more than 3 orders of magnitude higher than primary ice
770 production (Fig. 6d). The significant role of SIP stands out also on 30 January at altitudes below
771 2 km. It is, therefore, essential to consider SIP though BR in the feeder cloud, in order to
772 achieve the enhanced levels of ICNCs frequently observed within seeder-feeder events in the
773 alpine region. This is in agreement with the observational study of Ramelli et al. (2021) on an
774 ice-seeding case occurring in the region around Davos in the Swiss Alps. In this study, they
775 proposed that SIP though HM and BR were necessary to explain the elevated ICNCs in feeder
776 clouds.

777 A classification of the dominant type of precipitation was applied to the polarimetric data
778 collected by a weather radar deployed at the Kleine Scheidegg station (2061 m a.s.l.) during the
779 SE case between 30 and 31 January (supplement Fig. S6). In the derived time series we can
780 identify periods when individual ice crystals (not aggregated and not significantly rimed)
781 dominate over the entire precipitation column followed by periods when a clear stratification
782 is present with ice crystals aloft and mostly aggregates and rimed ice particles below. This
783 stratification is observed on 30 January at 19:00 UTC when the model tendencies are extracted
784 (dashed lines in Fig. 6). Allowing for the BR process in PHILL simulation results in a 2 orders
785 of magnitude enhancement in the aggregation rates close to the ground, which can better



786 reproduce the signatures observed in the hydrometeor classification at that time. An increase
787 in the simulated aggregates and rimed particles is expected to increase orographic precipitation,
788 which is important given that these low-level feeder clouds are incapable of producing
789 significant amounts of precipitation. Indeed, the mean surface precipitation produced by
790 PHILL is 30% (10%) increased during the NW (SE) case compared with CNTRL (Fig. S7),
791 which is in contrast to Dedekind et al. (2021) where the activation of the BR process is found
792 to suppress the regions of strong surface precipitation. This was attributed to the limited
793 efficiency of the small secondary ice particles to grow sufficiently to precipitation sizes when
794 the local updrafts lift them to the upper parts of the cloud that were glaciated. The radar-based
795 hydrometeor classification reveals also the predominance of ice crystals at the beginning and
796 the end of the precipitating periods (e.g., on 30 January at 15:00-17:30 or 31 January at 04:30-
797 06:00), which is again more consistent with the vertical profile of N_i produced by PHILL rather
798 than the CNTRL simulation (supplement Fig. S6, S8).

799

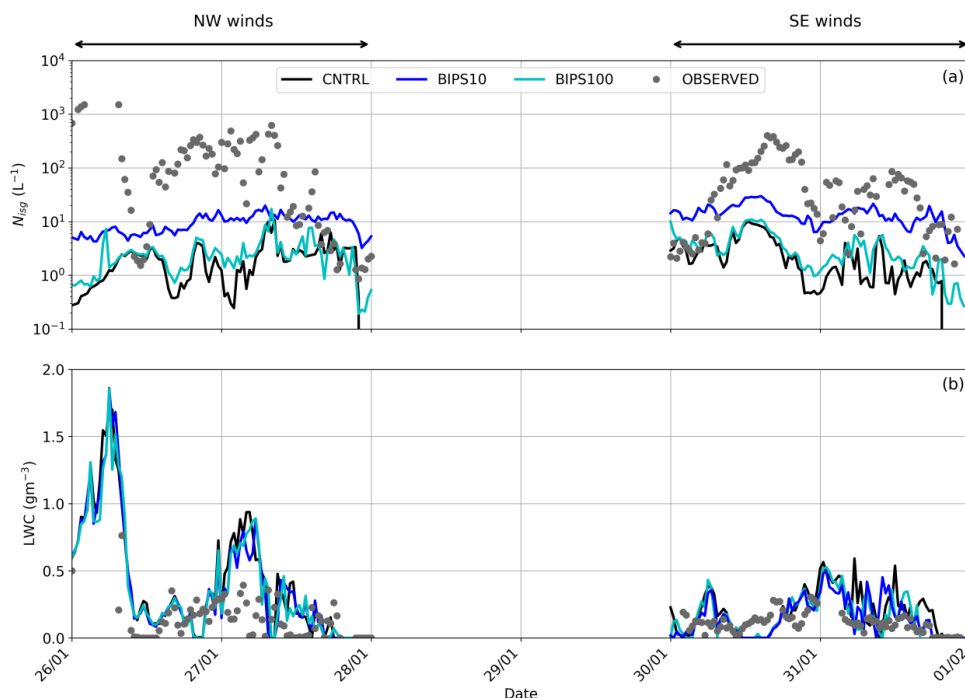
800 3.2 Sensitivity to the injection of ice crystals from the surface

801 In this section we examine if the surface-originating small ice particles could have the potential
802 to initiate and enhance ice particle growth in the near-surface MPCs present in our case studies.
803 Fig. 7 illustrates two additional WRF simulations – BIPS10 and BIPS100 – where the ice
804 crystal source applied to the first model level is equal to 10 and 100 L^{-1} , respectively (Table 2).
805 Note that these two sensitivity tests do not consider any SIP process to analyze the influence
806 of BIPS only. The total N_{isg} values produced in BIPS10 are only slightly increased compared
807 to the CNTRL simulation and generally remain outside the observed range at JFJ (Fig. 7a). An
808 order of magnitude increase in the applied NBIPS is seen to enhance the modeled N_{isg} during
809 both case studies, however our simulations are still lacking ice particles. This is particularly
810 evident during the NW winds case, where the simulated N_{isg} varies most of the time around 10
811 L^{-1} , remaining an order of magnitude lower than the observations. During the SE case, the
812 model performance is slightly improved with the N_{isg} reaching up to $\sim 25 L^{-1}$ in BIPS100, which
813 occasionally falls within the lower limit of the observed ICNC values (e.g., in the evening of
814 31 January). At times when the detected ICNCs remain quite low (i.e., on the order of $10 L^{-1}$),
815 the contribution of blowing snow particles probably from the Aletsch Glacier is sufficient to
816 explain the observations at JFJ.

817 As indicated in Fig. 7b, during the NW flow the simulated LWC at the first model level
818 in BIPS10 and BIPS100 almost coincides with the CNTRL simulation of WRF. The three
819 sensitivity simulations are producing comparable median and quartile LWC values (Table 5),



820 with BIPS10 and BIPS100 producing median LWC values closer to the observed ones during
821 the SE flow. When comparing against the LWC values in the third quartile though, the two
822 simulations lead to an overestimation up to a factor of ~ 1.5 during both case studies. Given that
823 there is approximately a factor of >20 (5) difference between the modeled and observed ICNCs
824 during the NW (SE) winds case (Table 3), Fig. 7 overall reveals that the addition of a source
825 of ice crystals from the effect of blowing snow cannot account for the observed liquid-ice phase
826 partitioning in the simulated orographic MPCs.
827



828
829 **Figure 7.** Time series of (a) total N_{isg} and (b) LWC, predicted between 26 January and 1
830 February 2014 by the two sensitivity simulations accounting for the effect of blowing snow,
831 BIPS10 (cyan line) and BIPS100 (blue line).

832

833 Our findings are in contrast with the modeling study of Farrington et al. (2016), where a
834 different approach was proposed to include the surface effect on the ICNCs simulated with
835 WRF. In this study, a single model domain was used with a horizontal resolution of 1 km. To
836 account for the flux of hoar crystals being detached from the surface by mechanical fracturing,
837 Farrington et al. (2016) included a wind-dependent surface flux of frost flowers adapted from
838 Xu et al. (2013). Despite the improved performance of the WRF model in terms of predicted



839 ICNCs and LWC, the wind-dependent formulation of the surface flux caused the modeled
840 ICNCs to become strongly correlated with the simulated horizontal wind speed – a behavior
841 that was not confirmed by the observations of Lloyd et al. (2015). Nonetheless, the highest
842 observed ICNCs at the beginning of the NW case correspond to the time when both the
843 observed and modeled wind speed is the strongest (Fig. 2c), implying that a wind-dependent
844 surface flux of BIPS could potentially elevate the simulated N_{isg} to the observed levels at this
845 time.

846

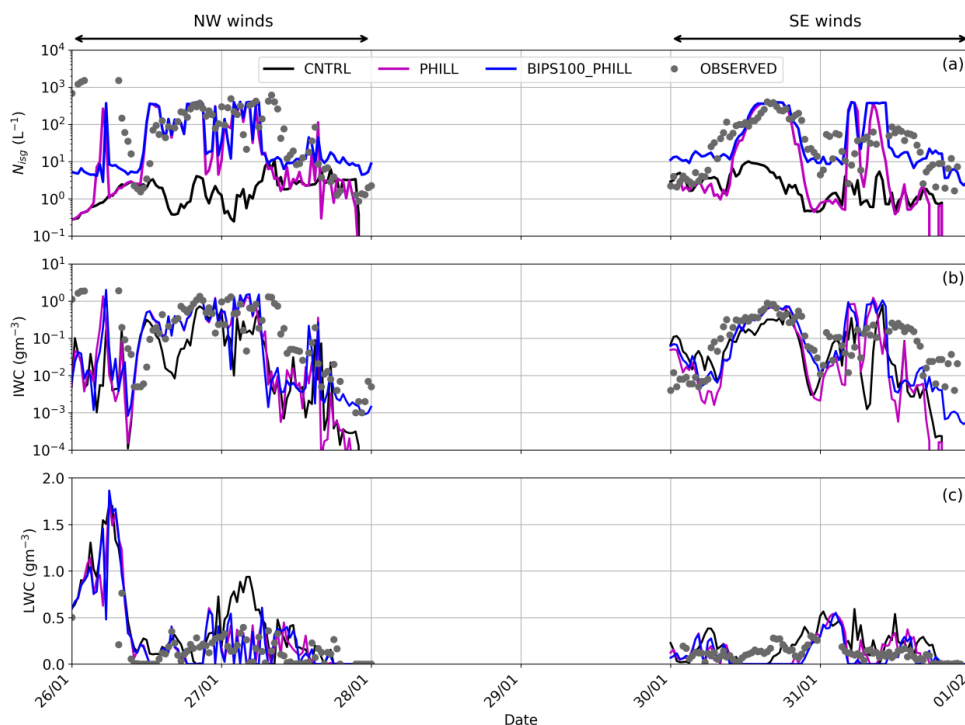
847 3.3 The synergistic impact of BR and surface-induced ice crystals

848 It is deducible from the above discussion that the sole inclusion of a constant source of BIPS
849 in our simulations cannot efficiently bridge the gap between modeled and measured ICNCs.
850 Our aim in this section is to explore the combined effect of SIP through BR and blowing snow
851 on the simulated orographic MPCs, since both processes are deemed to be important when
852 trying to explain the high ICNCs observed in alpine environments. This is addressed in the
853 final sensitivity simulation, BIPS100_PHILL, the results of which are compared with the
854 CNTRL and PHILL simulations in Fig. 8.

855 In terms of the modeled ice particle concentrations, the combination of the simplified
856 blowing snow treatment and BR parameterization can account for most of the discrepancy
857 between modeled and observed ICNCs, particularly during the SE case (Fig. 8a), when the
858 simulation leads to best agreement with the observed interquartile values (Table 3).
859 BIPS100_PHILL and CNTRL generally differ by an average factor of ~100 (40) during the
860 NW (SE) case, with the former producing N_{isg} values that are sometimes elevated by up to ~3
861 (2) orders of magnitude (Fig. 8a). Compared to PHILL setup, including a source of BIPS is
862 found to improve the modeled ICNCs close to the surface episodically – for instance in the
863 evening of 30 and 31 January, with the N_{isg} in BIPS100_PHILL efficiently reaching the
864 observed levels (Fig. 8a). Note that BIPS can contribute to the modeled N_{isg} even without the
865 presence of a near-surface orographic cloud (e.g., Geerts et al., 2015; Beck et al., 2018). For
866 instance, BIPS100_PHILL is the only sensitivity simulation producing high N_{isg} values in the
867 evening of 27 and 31 January, when the low-level cloud is dissipated (Fig. 5c, f). In the former
868 case, however, the model results in an overestimate of the ICNCs, which is also observed
869 during the early hours of 30 January, suggesting that the applied source of ice crystals is
870 unrealistically high at this time.



871 As the mixed-phase conditions are sustained throughout both case studies (Fig. 8c), the
872 plume of ice crystals is mixed into an ice-supersaturated environment and, thus, BIPS are
873 expected to promote ice growth through their interaction with the surrounding supercooled
874 liquid droplets and (ice) supersaturated air. The number of BIPS reaching the cloud base might
875 not be large, but their presence is expected to further facilitate the action of the BR mechanism,
876 considering the depositional growth they will undergo within the supercooled boundary layer
877 cloud. This is illustrated for example with the concurrent increase in N_{isg} and IWC observed on
878 30 January at approximately 21:00 UTC (Fig. 8a, 8b) in the presence of the low-level cloud
879 (Fig. 8c). Note that the elevated N_{isg} caused by the addition of BIPS is not always followed by
880 an efficient increase in the simulated IWC. This can be observed for example on 27 January at
881 12:00 UTC or in the evening of 31 January (Fig. 8b).
882



883
884 **Figure 8.** Time series of (a) total N_{isg} , (b) IWC and (c) LWC, predicted between 26 January
885 and 1 February 2014 by the sensitivity simulation BIPS100_PHILL (blue line), which
886 examines the combined effect of ice multiplication through BR and blowing snow.
887

888 A discrepancy between modeled and observed IWC was also highlighted in the study of
889 Farrington et al. (2016), and was attributed to the small sizes of the hoar frost particles assumed



890 (i.e., 10 μm). Although here BIPS are assumed to have sizes of 100 μm , still the
891 underestimation in the cloud IWC has not been overcome. This suggests that the applied source
892 of BIPS combined with the effect of SIP through BR shifts the ice particle spectra to smaller
893 sizes, which are not very efficient in riming and the WBF process and, thus, do not always
894 contribute to significant increases in IWC values. Overall, the interquartile values presented in
895 Table 4 reveal that BIPS100_PHILL and PHILL yield almost identical IWC values, suggesting
896 that the implementation of a constant source of BIPS does not further improve the
897 representation of the total ice mass despite the improvements in the simulated N_{isg} . Focusing
898 on the LWC values in the third quartile, though, including a source of BIPS results in better
899 agreement with the CLACE observations during the SE case, while it is shown to have little
900 effect on the cloud liquid phase during the NW case (Table 5). Despite the increase in the
901 modeled N_{isg} observed in BIPS100_PHILL especially during the SE case, the liquid water in
902 the low-level orographic cloud is not further depleted (Fig. 8c). This is presumably because the
903 mean surface precipitation produced is also enhanced by almost $\sim 20\%$ compared to PHILL
904 (supplement Fig. S7), which seems to balance the excessive ice production.

905 One final point that is worth noting here is that there are still some certain periods when
906 BIPS100_PHILL fails to reproduce the observed range of ICNCs. This could imply the
907 potential contribution of additional ice multiplication processes to the observed ice particle
908 concentrations. Indeed, the seeder-feeder configuration observed in the examined case studies
909 could favor the fragmentation of sublimating hydrometeors while falling through an
910 subsaturated environment before entering the feeder cloud (e.g., Bacon et al., 1998). The so-
911 called “sublimational break-up” is an overlooked SIP process which is not yet described in the
912 M05 scheme. Also, note that the periods when the modeled ICNCs remain below the observed
913 ice number levels are mainly identified when the simulated temperature drops below $-15\text{ }^{\circ}\text{C}$
914 and the wind speed exceeds 10 ms^{-1} or even 20 ms^{-1} (e.g., in the morning of 26 January or 27
915 January at around 12:00 UTC). This is when the incorporation of surface-based processes
916 becomes of primary importance. The simplified methodology we followed here although
917 instructive, yet it faces several limitations. For instance, the constant source of BIPS is
918 sometimes found to overestimate the modeled N_{isg} and IWC. In order to accurately assess the
919 potential role of the snow-covered surfaces in elevating the simulated ICNCs, an improved
920 spatio-temporal description of the concentration and distribution of BIPS is required.
921 Furthermore, the applied ice crystal source is independent of some key parameters controlling
922 its resuspension, such as the horizontal wind speed, the updrafts or the friction velocity (e.g.,
923 Vionnet et al., 2013, 2014). For example, in the early morning hours of 26 January, the high



924 simulated horizontal and vertical velocities (Fig. 2c, 2d) are expected to loft significant BIPS
925 concentrations into the cloud layer, owing to enhanced mechanical mixing and momentum flux
926 close to the surface. Nonetheless, the contribution of the induced plume of BIPS remains
927 constant throughout the NW case study (Fig. 7a), which seems to lead to an underestimation
928 of the total ice particle concentration and mass. A more realistic parameterization of the BIPS
929 flux or the coupling with a detailed snowpack model would, therefore, be essential for a more
930 accurate representation of the effect of blowing snow.

931

932 **4. Summary and conclusions**

933 This study employs the mesoscale model WRF to explore the potential impact of ice
934 multiplication processes on the liquid-ice phase partitioning in the orographic MPCs observed
935 during the CLACE 2014 campaign at the mountain-top site of JFJ in the Swiss Alps. The
936 orography surrounding JFJ channels the direction of the horizontal wind speed, giving us the
937 opportunity to analyze two frontal cases occurring under NW and SE conditions.

938 DS and BR mechanisms were implemented in the default M05 scheme in WRF, in
939 addition to the HM parameterization, which however remained inactive in the simulated
940 temperature range (-10 to -24 °C). The DS process is parameterized following either the latest
941 theoretical formulation developed by Phillips et al. (2018) or the more simplified
942 parameterization proposed by Sullivan et al. (2018a). Our sensitivity simulations revealed that
943 the DS mechanism is ineffective in the two considered alpine MPCs, even under the higher
944 updraft velocity conditions associated with the NW winds case study. This is due to a lack of
945 sufficiently big raindrops, necessary to initiate this process.

946 To parameterize the number of fragments generated per ice-ice collision we followed
947 again two different approaches: either the simplified temperature dependent formulation of
948 Takahashi et al. (1995) scaled for the size of the particle that undergo fragmentation
949 (Sotiropoulou et al., 2021a) or the more advanced physically-based Phillips et al. (2017a)
950 parameterization. Including a description of the BR mechanism is essential for reproducing the
951 ICNCs observed in the simulated orographic clouds, especially at temperatures higher than \sim
952 -15 °C, where INPs are generally sparse. SIP through BR is found to enhance the modeled
953 ICNCs by up to 3 (2) orders of magnitude during the NW (SE) case, improving the model
954 agreement with observations. This ice enhancement can cause up to an order of magnitude
955 increase in the mean simulated IWC values compared with the CNTRL simulation, which is



956 attributed to the enhanced ice crystal growth and cloud-ice-to-snow autoconversion. The
957 increase in the simulated ICNCs also depletes the cloud LWC by at least a factor of 2 during
958 both cases, which is more consistent with the measured LWC values.

959 One of the most interesting outcomes of this study is the association of the enhanced BR
960 efficiency with the occurrence of in-cloud seeder-feeder events, which are commonly found in
961 Switzerland (Proske et al., 2021). While ice-seeding situations are associated with enhanced
962 orographic precipitation in the alpine region, the CNTRL simulation fails to reproduce the
963 elevated ICNCs reaching the ground. The falling ice hydrometeors experience efficient growth
964 through aggregation in the seeder part of the cloud, which is enhanced when reaching the feeder
965 cloud at altitudes below 2 km, where primary ice crystals form and grow through vapor
966 deposition and riming. Aggregation of snowflakes seems to be the major driver of secondary
967 ice formation in the examined seeder-feeder events. SIP though BR is initiated already within
968 the seeder cloud, while it becomes immensely important in the feeder cloud where its
969 production rate exceeds the one of primary ice formation. The increased generation of
970 secondary ice fragments does not always lead to ice explosion and cloud glaciation, as it is
971 followed by an enhancement in the precipitation sink owing to a shift in the ice particle
972 spectrum. Including a description of the BR mechanism is, therefore, crucial for explaining the
973 ice particle concentration and mass observed in the low-level feeder clouds.

974 To assess the potential role of blowing snow in the simulated orographic clouds, a
975 constant source of ice crystals was introduced in the first atmospheric level of WRF. Our results
976 indicate that blowing snow alone cannot explain the high ICNCs observed at JFJ, but when this
977 source is combined with the BR mechanism then the gap between modeled and measured
978 ICNCs is sufficiently bridged. The biggest influence of blowing snow is mainly detected at
979 times when the simulated temperatures are low enough (< -15 °C), while the presence of a low-
980 level cloud is required for SIP to manifest. The concentrations of BIPS reaching the cloud base
981 are not high, but when they are mixed among supercooled liquid droplets they are expected to
982 grow, facilitating ice multiplication through BR. Nonetheless, including a wind-dependence or
983 a spatio-temporal variability in the applied ice crystal source would be essential to provide a
984 more precise description of the effect of blowing snow on the simulated clouds.

985 Overall, our findings indicate that outside the HM temperature range, a correct
986 representation of both secondary ice and an external ice seeding mechanism, which is primarily
987 precipitating ice particles formed aloft and to a lesser degree wind-blown ice from the surface,
988 will improve the accuracy of the liquid-ice partitioning in MPCs predicted by atmospheric



989 numerical models. More precisely, the implementation of SIP through BR can effectively shift
990 the number concentrations of ice particles in the right direction dictated by observations of
991 alpine MPCs, which is in turn critical not only for the determination of their optical properties
992 but also for the accurate estimate of precipitation patterns.

993

994 *Code and data availability.* The WRF outputs presented in this study will be made available at
995 <https://zenodo.org/>, while the updated Morrison scheme is available upon request. @Note by
996 authors: Data will be made available upon acceptance of final publication.

997

998 *Competing interests.* The authors declare no conflict of interest.

999

1000 *Author Contributions.* PG and AN conceived and led this study with input from GS. EV helped
1001 with the WRF configuration and setup. GS provided the updated microphysics scheme with
1002 the detailed BR parameterizations. PG implemented the DS parameterizations with help from
1003 GS, conducted the simulations, analyzed the results and, together with AN, wrote the main
1004 paper. All authors contributed to the scientific interpretation and writing of the paper.

1005

1006 *Acknowledgements.* The authors would like to thank Gary Lloyd for providing the
1007 microphysical measurements, as well as Jacopo Grazioli for collecting and pre-processing the
1008 radar data. The authors are also thankful to Varun Sharma and Michael Lehning for the fruitful
1009 discussions on the contribution of blowing snow in the alpine region.

1010

1011 *Financial support.* This research has been supported by the Horizon 2020 project FORCeS
1012 (grant 821205) and the European Research Council project PyroTRACH (grant 726165). GS
1013 received funding from the Swedish Research Council for Sustainable Development FORMAS
1014 (project ID 2018-01760).

1015



1016 **References**

- 1017 Atlas, R. L., Bretherton, C. S., Blossey, P. N., Gettelman, A., Bardeen, C., Lin, P. and Ming,
1018 Y.: How Well Do Large-Eddy Simulations and Global Climate Models Represent
1019 Observed Boundary Layer Structures and Low Clouds Over the Summertime Southern
1020 Ocean?, *J. Adv. Model. Earth Syst.*, 12(11), 1–25, doi:10.1029/2020MS002205, 2020.
- 1021 Baltensperger, U., Schwikowski, M., Jost, D. T., Nyeki, S., Gäggeler, H. W. and Poulida, O.:
1022 Scavenging of atmospheric constituents in mixed phase clouds at the high-alpine site
1023 Jungfraujoch part I: Basic concept and aerosol scavenging by clouds, *Atmos. Environ.*, 32,
1024 3975–3983, doi:10.1016/S1352-2310(98)00051-X, 1998.
- 1025 Beck, A., Henneberger, J., Fugal, J. P., David, R. O., Lacher, L. and Lohmann, U.: Impact of
1026 surface and near-surface processes on ice crystal concentrations measured at mountain-top
1027 research stations, *Atmos. Chem. Phys.*, 18(12), 8909–8927, doi:10.5194/acp-18-8909-
1028 2018, 2018.
- 1029 Beheng, K. D.: Microphysical Properties of Glaciating Cumulus Clouds: Comparison of
1030 Measurements With A Numerical Simulation, *Q. J. R. Meteorol. Soc.*, 113(478), 1377–
1031 1382, doi:10.1002/qj.49711347815, 1987.
- 1032 Bergeron, T.: On the physics of clouds and precipitation, *Proc. 5th Assembly UGGI*, 1935,
1033 Lisbon, Portugal, 156–180, 1935.
- 1034 Bigg, E. K.: The supercooling of water, *Proc. Phys. Soc. Sect. B*, 66(8), 688–694,
1035 doi:10.1088/0370-1301/66/8/309, 1953.
- 1036 Brown, P. R. A. and Francis, P. N.: Improved Measurements of the Ice Water Content in Cirrus
1037 Using a Total-Water Probe, *J. Atmos. Ocean. Technol.*, 12, 410–414, doi:10.1175/1520-
1038 0426(1995)012<0410:IMOTIW>2.0.CO;2, 1995.
- 1039 Browning, K. A., Hill, F. F. and Pardoe, C. W.: Structure and mechanism of precipitation and
1040 the effect of orography in a wintertime warm sector, *Q. J. R. Meteorol. Soc.*, 100(425),
1041 309–330, doi:10.1002/qj.49710042505, 1974.
- 1042 Browning, K. A., Pardoe, C. W. and Hill, F. F.: The nature of orographic rain at wintertime
1043 cold fronts, *Q. J. R. Meteorol. Soc.*, 101(428), 333–352, doi:10.1002/qj.49710142815,
1044 1975.
- 1045 Chen, F. and Dudhia, J.: Coupling and advanced land surface-hydrology model with the Penn
1046 State-NCAR MM5 modeling system. Part I: Model implementation and sensitivity, *Mon.*
1047 *Weather Rev.*, 129(4), 569–585, doi:10.1175/1520-
1048 0493(2001)129<0569:CAALSH>2.0.CO;2, 2001.



- 1049 Chou, C., Stetzer, O., Weingartner, E., Jurányi, Z., Kanji, Z. A. and Lohmann, U.: Ice nuclei
1050 properties within a Saharan dust event at the Jungfraujoch in the Swiss Alps, *Atmos.*
1051 *Chem. Phys.*, 11, 4725–4738, doi:10.5194/acp-11-4725-2011, 2011.
- 1052 Choulaton, T. W., Griggs, D. J., Humood, B. Y. and Latham, J.: Laboratory studies of riming,
1053 and its relation to ice splinter production, *Q. J. R. Meteorol. Soc.*, 106(448), 367–374,
1054 doi:10.1002/qj.49710644809, 1980.
- 1055 Choulaton, T. W., Bower, K. N., Weingartner, E., Crawford, I., Coe, H., Gallagher, M. W.,
1056 Flynn, M., Crosier, J., Connolly, P., Targino, A., Alfarra, M. R., Baltensperger, U.,
1057 Sjogren, S., Verheggen, B., Cozic, J. and Gysel, M.: The influence of small aerosol
1058 particles on the properties of water and ice clouds, *Faraday Discuss.*, 137, 205–222,
1059 doi:10.1039/b702722m, 2008.
- 1060 Chow, F. K., De Wekker, Stephan, F. J., and Snyder, B. J.: Mountain weather research and
1061 forecasting: recent progress and current challenges, Springer, Dordrecht, the Netherlands,
1062 2013.
- 1063 Conen, F., Rodríguez, S., Hüglin, C., Henne, S., Herrmann, E., Bukowiecki, N. and Alewell,
1064 C.: Atmospheric ice nuclei at the high-altitude observatory Jungfraujoch, Switzerland,
1065 *Tellus, Ser. B Chem. Phys. Meteorol.*, 67(1), doi:10.3402/tellusb.v67.25014, 2015.
- 1066 Cooper, W. A.: Ice initiation in natural clouds, *Meteor. Mon.*, 21, 29–32,
1067 <https://doi.org/10.1175/0065-9401-21.43.29>, 1986.
- 1068 Crosier, J., Bower, K. N., Choulaton, T. W., Westbrook, C. D., Connolly, P. J., Cui, Z. Q.,
1069 Crawford, I. P., Capes, G. L., Coe, H., Dorsey, J. R., Williams, P. I., Illingworth, A. J.,
1070 Gallagher, M. W. and Blyth, A. M.: Observations of ice multiplication in a weakly
1071 convective cell embedded in supercooled mid-level stratus, *Atmos. Chem. Phys.*, 11(1),
1072 257–273, doi:10.5194/acp-11-257-2011, 2011.
- 1073 Dedekind, Z., Lauber, A., Ferrachat, S. and Lohmann, U.: Sensitivity of precipitation formation
1074 to secondary ice production in winter orographic mixed-phase clouds, *Atmos. Chem. Phys.*
1075 *Discuss.*, (February), 1–27, doi:10.5194/acp-2020-1326, 2021.
- 1076 Déry, S. J. and Yau, M. K.: A climatology of adverse winter-type weather events, *J. Geophys.*
1077 *Res. Atmos.*, 104(D14), 16657–16672, doi:10.1029/1999JD900158, 1999.
- 1078 Farrington, R. J., Connolly, P. J., Lloyd, G., Bower, K. N., Flynn, M. J., Gallagher, M. W.,
1079 Field, P. R., Dearden, C. and Choulaton, T. W.: Comparing model and measured ice
1080 crystal concentrations in orographic clouds during the INUPIAQ campaign, *Atmos. Chem.*
1081 *Phys.*, 16(8), 4945–4966, doi:10.5194/acp-16-4945-2016, 2016.
- 1082 Field, P. R. and Heymsfield, A. J.: Importance of snow to global precipitation, *Geophys. Res.*



- 1083 Lett., 42(21), 9512–9520, doi:10.1002/2015GL065497, 2015.
- 1084 Field, P. R., Lawson, R. P., Brown, P. R. A., Lloyd, G., Westbrook, C., Moisseev, D.,
1085 Miltenberger, A., Nenes, A., Blyth, A., Choulaton, T., Connolly, P., Buehl, J., Crosier, J.,
1086 Cui, Z., Dearden, C., DeMott, P., Flossmann, A., Heymsfield, A., Huang, Y., Kalesse, H.,
1087 Kanji, Z. A., Korolev, A., Kirchgaessner, A., Lasher-Trapp, S., Leisner, T., McFarquhar,
1088 G., Phillips, V., Stith, J. and Sullivan, S.: Chapter 7. Secondary Ice Production - current
1089 state of the science and recommendations for the future, *Meteorol. Monogr.*, 58,
1090 doi:10.1175/amsmonographs-d-16-0014.1, 2017.
- 1091 Findeisen, W.: Die kolloidmeteorologischen vorgänge bei der niederschlagsbildung, *Meteorol.*
1092 *Z.*, 55, 121–133, 1938.
- 1093 Fridlind, A. M., Ackerman, A. S., McFarquhar, G., Zhang, G., Poellot, M. R., DeMott, P. J.,
1094 Prenni, A. J. and Heymsfield, A. J.: Ice properties of single-layer stratocumulus during the
1095 Mixed-Phase Arctic Cloud Experiment: 2. Model results, *J. Geophys. Res. Atmos.*,
1096 112(24), 1–25, doi:10.1029/2007JD008646, 2007.
- 1097 Fu, S., Deng, X., Shupe, M. D. and Xue, H.: A modelling study of the continuous ice formation
1098 in an autumnal Arctic mixed-phase cloud case, *Atmos. Res.*, 228(March), 77–85,
1099 doi:10.1016/j.atmosres.2019.05.021, 2019.
- 1100 Geerts, B., Pokharel, B. and Kristovich, D. A. R.: Blowing snow as a natural glaciogenic cloud
1101 seeding mechanism, *Mon. Weather Rev.*, 143(12), 5017–5033, doi:10.1175/MWR-D-15-
1102 0241.1, 2015.
- 1103 Grazioli, J., Lloyd, G., Panziera, L., Hoyle, C. R., Connolly, P. J., Henneberger, J. and Berne,
1104 A.: Polarimetric radar and in situ observations of riming and snowfall microphysics during
1105 CLACE 2014, *Atmos. Chem. Phys.*, 15, 13787–13802, doi:10.5194/acp-15-13787-2015,
1106 2015.
- 1107 Griggs, D. J. and Choulaton, T. W.: Freezing modes of riming droplets with application to ice
1108 splinter production, *Q. J. R. Meteorol. Soc.*, 109(459), 243–253,
1109 doi:10.1002/qj.49710945912, 1983.
- 1110 Griggs, D. J. and Choulaton, T. W.: A laboratory study of secondary ice particle production
1111 by the fragmentation of rime and vapour-grown ice crystals, *Q. J. R. Meteorol. Soc.*,
1112 112(471), 149–163, doi:10.1256/smsqj.47108, 1986.
- 1113 Hallett, J. and Mossop, S. C.: Production of secondary ice particles during the riming process,
1114 *Nature*, 249, 26–28, doi:10.1038/249026a0, 1974.
- 1115 Harris, L. M. and Durran, D. R.: An Idealized Comparison of One-Way and Two-Way Grid
1116 Nesting, *Mon. Weather Rev.*, 138(6), 2174–2187, doi:10.1175/2010MWR3080.1, 2010.



- 1117 Henneberg, O., Henneberger, J. and Lohmann, U.: Formation and development of orographic
1118 mixed-phase clouds, *J. Atmos. Sci.*, 74(11), 3703–3724, doi:10.1175/JAS-D-16-0348.1,
1119 2017.
- 1120 Hersbach, H., Bell, B., Berrisford, P., Hirahara, S., Horányi, A., Muñoz-Sabater, J., Nicolas,
1121 J., Peubey, C., Radu, R., Schepers, D., Simmons, A., Soci, C., Abdalla, S., Abellan, X.,
1122 Balsamo, G., Bechtold, P., Biavati, G., Bidlot, J., Bonavita, M., De Chiara, G., Dahlgren,
1123 P., Dee, D., Diamantakis, M., Dragani, R., Flemming, J., Forbes, R., Fuentes, M., Geer,
1124 A., Haimberger, L., Healy, S., Hogan, R. J., Hólm, E., Janisková, M., Keeley, S., Laloyaux,
1125 P., Lopez, P., Lupu, C., Radnoti, G., de Rosnay, P., Rozum, I., Vamborg, F., Villaume, S.
1126 and Thépaut, J. N.: The ERA5 global reanalysis, *Q. J. R. Meteorol. Soc.*, 146(730), 1999–
1127 2049, doi:10.1002/qj.3803, 2020.
- 1128 Heymsfield, A. J. and Mossop, S. C.: Temperature dependence of secondary ice crystal
1129 production during soft hail growth by riming, *Q. J. R. Meteorol. Soc.*, 110(465), 765–770,
1130 doi:10.1002/qj.49711046512, 1984.
- 1131 Heymsfield, A. J., Schmitt, C., Bansemer, A. and Twohy, C. H.: Improved representation of
1132 ice particle masses based on observations in natural clouds, *J. Atmos. Sci.*, 67(10), 3303–
1133 3318, doi:10.1175/2010JAS3507.1, 2010.
- 1134 Hoarau, T., Pinty, J. P. and Barthe, C.: A representation of the collisional ice break-up process
1135 in the two-moment microphysics LIMA v1.0 scheme of Meso-NH, *Geosci. Model Dev.*,
1136 11(10), 4269–4289, doi:10.5194/gmd-11-4269-2018, 2018.
- 1137 Hoose, C. and Möhler, O.: Heterogeneous ice nucleation on atmospheric aerosols: A review of
1138 results from laboratory experiments., 2012.
- 1139 James, R. L., Phillips, V. T. J., and Connolly, P. J.: Secondary ice production during the break-
1140 up of freezing water drops on impact with ice particles, *Atmos. Chem. Phys. Discuss.*
1141 [preprint], <https://doi.org/10.5194/acp-2021-557>, in review, 2021.
- 1142 Janjić, Z. I.: Nonsingular Implementation of the Mellor-Yamada Level 2.5 Scheme in the
1143 NCEP Meso model, NOAA/NWS/NCEP Off. note 437, 61 pp, 2002.
- 1144 Ikawa, M. and Saito, K.: Description of a Non-hydrostatic Model Developed at the Forecast
1145 Research Department of the MR, MRI Tech. Rep. 28, 238 pp., 1991.
- 1146 Kanji, Z. A., Ladino, L. A., Wex, H., Boose, Y., Burkert-Kohn, M., Cziczo, D. J. and Krämer,
1147 M.: Overview of Ice Nucleating Particles, *Meteorol. Monogr.*, 58, 1.1-1.33,
1148 doi:10.1175/amsmonographs-d-16-0006.1, 2017.
- 1149 Keinert, A., Spannagel, D., Leisner, T. and Kiselev, A.: Secondary ice production upon
1150 freezing of freely falling drizzle droplets, *J. Atmos. Sci.*, 77(8), 2959–2967,



- 1151 doi:10.1175/JAS-D-20-0081.1, 2020.
- 1152 Ketterer, C., Zieger, P., Bukowiecki, N., Collaud Coen, M., Maier, O., Ruffieux, D. and
1153 Weingartner, E.: Investigation of the Planetary Boundary Layer in the Swiss Alps Using
1154 Remote Sensing and In Situ Measurements, *Boundary-Layer Meteorol.*, 151(2), 317–334,
1155 doi:10.1007/s10546-013-9897-8, 2014.
- 1156 Kleinheins, J., Kiselev, A., Keinert, A., Kind, M. and Leisner, T.: Thermal imaging of freezing
1157 drizzle droplets: pressure release events as a source of secondary ice particles, *J. Atmos.*
1158 *Sci.*, 1–28, doi:10.1175/jas-d-20-0323.1, 2021.
- 1159 Korolev, A. and Isaac, G.: Phase transformation of mixed-phase clouds, *Q. J. R. Meteorol.*
1160 *Soc.*, 129(587 PART A), 19–38, doi:10.1256/qj.01.203, 2003.
- 1161 Korolev, A. and Leisner, T.: Review of experimental studies of secondary ice production.,
1162 2020.
- 1163 Korolev, A., McFarquhar, G., Field, P. R., Franklin, C., Lawson, P., Wang, Z., Williams, E.,
1164 Abel, S. J., Axisa, D., Borrmann, S., Crosier, J., Fugal, J., Krämer, M., Lohmann, U.,
1165 Schlenczek, O., Schnaiter, M. and Wendisch, M.: Mixed-Phase Clouds: Progress and
1166 Challenges, *Meteorol. Monogr.*, 58, 5.1-5.50, doi:10.1175/amsmonographs-d-17-0001.1,
1167 2017.
- 1168 Korolev, A., Heckman, I., Wolde, M., Ackerman, A. S., Fridlind, A. M., Ladino, L. A., Paul
1169 Lawson, R., Milbrandt, J. and Williams, E.: A new look at the environmental conditions
1170 favorable to secondary ice production, *Atmos. Chem. Phys.*, 20(3), 1391–1429,
1171 doi:10.5194/acp-20-1391-2020, 2020.
- 1172 Korolev, A. V., Emery, E. F., Strapp, J. W., Cober, S. G., Isaac, G. A., Wasey, M. and Marcotte,
1173 D.: Small ice particles in tropospheric clouds: Fact or artifact? Airborne icing
1174 instrumentation evaluation experiment, *Bull. Am. Meteorol. Soc.*, 92(8), 967–973,
1175 doi:10.1175/2010BAMS3141.1, 2011.
- 1176 Lance, S., Brock, C. A., Rogers, D. and Gordon, J. A.: Water droplet calibration of the Cloud
1177 Droplet Probe (CDP) and in-flight performance in liquid, ice and mixed-phase clouds
1178 during ARCPAC, *Atmos. Meas. Tech.*, 3(6), 1683–1706, doi:10.5194/amt-3-1683-2010,
1179 2010.
- 1180 Latham, J. and Warwicker, R.: Charge transfer accompanying the splashing of supercooled
1181 raindrops on hailstones, *Q. J. R. Meteorol. Soc.*, 106(449), 559–568,
1182 doi:10.1002/qj.49710644912, 1980.
- 1183 Lauber, A., Kiselev, A., Pander, T., Handmann, P. and Leisner, T.: Secondary ice formation
1184 during freezing of levitated droplets, *J. Atmos. Sci.*, 75(8), 2815–2826, doi:10.1175/JAS-



- 1185 D-18-0052.1, 2018.
- 1186 Lauber, A., Henneberger, J., Mignani, C., Ramelli, F., Pasquier, J. T., Wieder, J., Hervo, M.
1187 and Lohmann, U.: Continuous secondary-ice production initiated by updrafts through the
1188 melting layer in mountainous regions, *Atmos. Chem. Phys.*, 21(5), 3855–3870,
1189 doi:10.5194/acp-21-3855-2021, 2021.
- 1190 Lawson, R. P., O’Connor, D., Zmarzly, P., Weaver, K., Baker, B., Mo, Q. and Jonsson, H.:
1191 The 2D-S (stereo) probe: Design and preliminary tests of a new airborne, high-speed, high-
1192 resolution particle imaging probe, *J. Atmos. Ocean. Technol.*, 23(11), 1462–1477,
1193 doi:10.1175/JTECH1927.1, 2006.
- 1194 Lawson, R. P., Woods, S. and Morrison, H.: The microphysics of ice and precipitation
1195 development in tropical cumulus clouds, *J. Atmos. Sci.*, 72(6), 2429–2445,
1196 doi:10.1175/JAS-D-14-0274.1, 2015.
- 1197 Lehning, M., I.Volksch, D.Gustafsson, Nguyen, T. A., Stahli, M. and Zappa, M.: ALPINE3D:
1198 A detailed model of mountain surface processes and its application to snow hydrology.,
1199 *Hydrol. Process.*, 20, 2111–2128, doi:10.1002/hyp.6204, 2006.
- 1200 Leisner, T., Pander, T., Handmann, P., and Kiselev, A.: Secondary ice processes upon
1201 heterogeneous freezing of cloud droplets, 14th Conf. on Cloud Physics and Atmospheric
1202 Radiation, Amer. Meteor. Soc, Boston, MA, 7 July 2014, available at:
1203 <https://ams.confex.com/ams/14CLOUD14ATRAD/webprogram/Paper250221.html> (last
1204 access: 9 November 2019), 2014.
- 1205 Lloyd, G., Choulaton, T. W., Bower, K. N., Gallagher, M. W., Connolly, P. J., Flynn, M.,
1206 Farrington, R., Crosier, J., Schlenzcek, O., Fugal, J. and Henneberger, J.: The origins of
1207 ice crystals measured in mixed-phase clouds at the high-alpine site Jungfrauoch, *Atmos.*
1208 *Chem. Phys.*, 15(22), 12953–12969, doi:10.5194/acp-15-12953-2015, 2015.
- 1209 Lohmann, U., Henneberger, J., Henneberg, O., Fugal, J. P., Bühl, J. and Kanji, Z. A.:
1210 Persistence of orographic mixed-phase clouds, *Geophys. Res. Lett.*, 43(19), 10,512-
1211 10,519, doi:10.1002/2016GL071036, 2016.
- 1212 Lowenthal, D. H., Hallar, A. G., David, R. O., Mccubbin, I. B., Borys, R. D. and Mace, G. G.:
1213 Mixed-phase orographic cloud microphysics during StormVEx and IFRACS, *Atmos.*
1214 *Chem. Phys.*, 19(8), 5387–5401, doi:10.5194/acp-19-5387-2019, 2019.
- 1215 Luke, E. P., Yang, F., Kollias, P., Vogelmann, A. M. and Maahn, M.: New insights into ice
1216 multiplication using remote-sensing observations of slightly supercooled mixed-phase
1217 clouds in the Arctic, *Proc. Natl. Acad. Sci. U. S. A.*, 118(13), 1–9,
1218 doi:10.1073/pnas.2021387118, 2021.



- 1219 Mahesh, A., Eager, R., Campbell, J. R. and Spinhirne, J. D.: Observations of blowing snow at
1220 the South Pole, *J. Geophys. Res. Atmos.*, 108(22), 1–9, doi:10.1029/2002jd003327, 2003.
- 1221 Meyers, M. P., DeMott, P. J. and Cotton, W. R.: New Primary Ice-Nucleation
1222 Parameterizations in an Explicit Cloud Model, *J. Appl. Meteorol.*, 31, 708–721,
1223 doi:10.1175/1520-0450(1992)031<0708:NPINPI>2.0.CO;2, 1992.
- 1224 Mignani, C., Creamean, J. M., Zimmermann, L., Alewell, C. and Conen, F.: New type of
1225 evidence for secondary ice formation at around -15 °c in mixed-phase clouds, *Atmos.*
1226 *Chem. Phys.*, 19(2), 877–886, doi:10.5194/acp-19-877-2019, 2019.
- 1227 Morrison, H., Curry, J. A. and Khvorostyanov, V. I.: A new double-moment microphysics
1228 parameterization for application in cloud and climate models. Part I: Description, *J. Atmos.*
1229 *Sci.*, 62, 1678–1693, doi:10.1175/JAS3446.1, 2005.
- 1230 Morrison, H. and Grabowski, W. W.: A novel approach for representing ice microphysics in
1231 models: Description and tests using a kinematic framework, *J. Atmos. Sci.*, 65(5),
1232 doi:10.1175/2007JAS2491.1, 2008.
- 1233 Morrison, H., De Boer, G., Feingold, G., Harrington, J., Shupe, M. D. and Sulia, K.: Resilience
1234 of persistent Arctic mixed-phase clouds, *Nat. Geosci.*, 5(1), 11–17, doi:10.1038/ngeo1332,
1235 2012.
- 1236 Mott, R., Scipi3n, D., Schneebeli, M., Dawes, N., Berne, A. and Lehning, M.: Orographic
1237 effects on snow deposition patterns in mountainous terrain, *J. Geophys. Res.*, 119(3),
1238 1419–1439, doi:10.1002/2013JD019880, 2014.
- 1239 M3lmenst3dtt, J., Sourdeval, O., Delano3e, J. and Quaas, J.: Frequency of occurrence of rain
1240 from liquid-, mixed-, and ice-phase clouds derived from A-Train satellite retrievals,
1241 *Geophys. Res. Lett.*, 42(15), 6502–6509, doi:10.1002/2015GL064604, 2015.
- 1242 Panziera, L. and Hoskins, B.: Large snowfall events in the south-eastern Alps, *Weather*, 63(4),
1243 88–93, doi:10.1002/wea.178, 2008.
- 1244 Phillips, V. T. J., Blyth, A. M., Brown, P. R. A., Choularton, T. W. and Latham, J.: The
1245 glaciation of a cumulus cloud over New Mexico, *Q. J. R. Meteorol. Soc.*, 127(575), 1513–
1246 1534, doi:10.1256/smsqj.57502, 2001.
- 1247 Phillips, V. T. J., Yano, J. I. and Khain, A.: Ice multiplication by breakup in ice-ice collisions.
1248 Part I: Theoretical formulation, *J. Atmos. Sci.*, 74(6), 1705–1719, doi:10.1175/JAS-D-16-
1249 0224.1, 2017a.
- 1250 Phillips, V. T. J., Yano, J. I., Formenton, M., Ilotoviz, E., Kanawade, V., Kudzotsa, I., Sun, J.,
1251 Bansemmer, A., Detwiler, A. G., Khain, A. and Tessorndorf, S. A.: Ice multiplication by
1252 breakup in ice-ice collisions. Part II: Numerical simulations, *J. Atmos. Sci.*, 74(9), 2789–



- 1253 2811, doi:10.1175/JAS-D-16-0223.1, 2017b.
- 1254 Phillips, V. T. J., Patade, S., Gutierrez, J. and Bansemmer, A.: Secondary ice production by
1255 fragmentation of freezing drops: Formulation and theory, *J. Atmos. Sci.*, 75(9), 3031–
1256 3070, doi:10.1175/JAS-D-17-0190.1, 2018.
- 1257 Proske, U., Bessenbacher, V., Dedekind, Z., Lohmann, U. and Neubauer, D.: How frequent is
1258 natural cloud seeding from ice cloud layers (<-35°C) over Switzerland?, *Atmos. Chem.*
1259 *Phys.*, 21(6), 5195–5216, doi:10.5194/acp-21-5195-2021, 2021.
- 1260 Pruppacher, H. R. and Klett, J. D.: *Microphysics of Clouds and Precipitation*, 2nd Edition,
1261 Kluwer Academic, Dordrecht, 954 pp., 1997.
- 1262 Purdy, J. C., Austin, G. L., Seed, A. W. and Cluckie, I. D.: Radar evidence of orographic
1263 enhancement due to the seeder feeder mechanism, *Meteorol. Appl.*, 12(3), 199–206,
1264 doi:10.1017/S1350482705001672, 2005.
- 1265 Qu, Y., Khain, A., Phillips, V., Ilotoviz, E., Shpund, J., Patade, S. and Chen, B.: The Role of
1266 Ice Splintering on Microphysics of Deep Convective Clouds Forming Under Different
1267 Aerosol Conditions: Simulations Using the Model With Spectral Bin Microphysics, *J.*
1268 *Geophys. Res. Atmos.*, 125(3), 1–23, doi:10.1029/2019JD031312, 2020.
- 1269 Ramelli, F., Henneberger, J., David, R., Bühl, J., Radenz, M., Seifert, P., Wieder, J., Lauber,
1270 A., Pasquier, J., Engelmann, R., Mignani, C., Hervo, M. and Lohmann, U.: Microphysical
1271 investigation of the seeder and feeder region of an Alpine mixed-phase cloud, *Atmos.*
1272 *Chem. Phys.*, 21, 6681–6706, doi:10.5194/acp-21-6681-2021, 2021.
- 1273 Rangno, A. L. and Hobbs, P. V.: Ice particles in stratiform clouds in the Arctic and possible
1274 mechanisms for the production of high ice concentrations, *J. Geophys. Res. Atmos.*,
1275 106(D14), 15065–15075, doi:10.1029/2000JD900286, 2001.
- 1276 Rasmussen, R. M., Geresdi, I., Thompson, G., Manning, K. and Karplus, E.: Freezing drizzle
1277 formation in stably stratified layer clouds: The role of radiative cooling of cloud droplets,
1278 cloud condensation nuclei, and ice initiation, *J. Atmos. Sci.*, 59(4), 837–860,
1279 doi:10.1175/1520-0469(2002)059<0837:FDFISS>2.0.CO;2, 2002.
- 1280 Reinking, R. F., Snider, J. B. and Coen, J. L.: Influences of storm-embedded orographic gravity
1281 waves on cloud liquid water and precipitation, *J. Appl. Meteorol.*, 39(6), 733–759,
1282 doi:10.1175/1520-0450(2000)039<0733:IOSEOG>2.0.CO;2, 2000.
- 1283 Reisner, J., Rasmussen, R. M. and Bruintjes, R. T.: Explicit forecasting of supercooled liquid
1284 water in winter storms using the MM5 mesoscale model, *Q. J. R. Meteorol. Soc.*, 124(548),
1285 1071–1107, doi:10.1002/qj.49712454804, 1998.
- 1286 Roe, G. H.: Orographic Precipitation, *Annu. Rev. Earth Planet. Sci.*, 33, 645–671,



- 1287 doi:10.1146/annurev.earth.33.092203.122541, 2005.
- 1288 Rogers, D. C. and Vali, G.: Ice Crystal Production by Mountain Surfaces, *J. Clim. Appl.*
1289 *Meteorol.*, 26, 1152–1168, doi:10.1175/1520-0450(1987)026<1152:ICPBMS>2.0.CO;2,
1290 1987.
- 1291 Rotunno, R. and Houze, R. A.: Lessons on orographic precipitation from the Mesoscale Alpine
1292 Programme, *Q. J. R. Meteorol. Soc.*, 133, 811–830, doi:10.1002/qj.67, 2007.
- 1293 Schlenczek, O., J. P. Fugal, K. N. Bower, J. Crosier, M. J. Flynn, G. Lloyd, and S. Borrmann,
1294 2014: Properties of pure ice clouds in an alpine environment. 14th Conf. on Cloud Physics,
1295 Boston, MA, Amer. Meteor. Soc. [Available online at
1296 [https://ams.confex.com/ams/14CLOUD14ATRAD/webprogram/Manuscript/Paper25030](https://ams.confex.com/ams/14CLOUD14ATRAD/webprogram/Manuscript/Paper250304/Schlenczek_et_al_2014_AMS_extended_abstract_klein.pdf)
1297 [4/Schlenczek_et_al_2014_AMS_extended_abstract_klein.pdf](https://ams.confex.com/ams/14CLOUD14ATRAD/webprogram/Manuscript/Paper250304/Schlenczek_et_al_2014_AMS_extended_abstract_klein.pdf).]
- 1298 Schmidt, R. A.: Measuring particle size and snowfall intensity in drifting snow., *Cold Reg. Sci.*
1299 *Technol.*, 9, 121–129, doi:10.1016/0165-232X(84)90004-1, 1984.
- 1300 Schwarzenboeck, A., Shcherbakov, V., Lefevre, R., Gayet, J. F., Pointin, Y. and Duroure, C.:
1301 Indications for stellar-crystal fragmentation in Arctic clouds, *Atmos. Res.*, 92(2), 220–228,
1302 doi:10.1016/j.atmosres.2008.10.002, 2009.
- 1303 Sotiropoulou, G., Sullivan, S., Savre, J., Lloyd, G., Lachlan-Cope, T., Ekman, A. M. L. and
1304 Nenes, A.: The impact of secondary ice production on Arctic stratocumulus, *Atmos. Chem.*
1305 *Phys.*, 20, 1301–1316, doi:10.5194/acp-20-1301-2020, 2020.
- 1306 Sotiropoulou, G., Vignon, E., Young, G., Morrison, H., O’Shea, S. J., Lachlan-Cope, T., Berne,
1307 A. and Nenes, A.: Secondary ice production in summer clouds over the Antarctic coast:
1308 An underappreciated process in atmospheric models, *Atmos. Chem. Phys.*, 21(2), 755–
1309 771, doi:10.5194/acp-21-755-2021, 2021a.
- 1310 Sotiropoulou, G., Ickes, L., Nenes, A. and Ekman, A.: Ice multiplication from ice–ice collisions
1311 in the high Arctic: sensitivity to ice habit, rimed fraction, ice type and uncertainties in the
1312 numerical description of the process, *Atmos. Chem. Phys.*, 21, 9741–9760,
1313 doi:10.5194/acp-21-9741-2021, 2021b.
- 1314 Sullivan, S. C., Hoose, C., Kiselev, A., Leisner, T. and Nenes, A.: Initiation of secondary ice
1315 production in clouds, *Atmos. Chem. Phys.*, 18(3), 1593–1610, doi:10.5194/acp-18-1593-
1316 2018, 2018a.
- 1317 Sullivan, S. C., Barthlott, C., Crosier, J., Zhukov, I., Nenes, A. and Hoose, C.: The effect of
1318 secondary ice production parameterization on the simulation of a cold frontal rainband,
1319 *Atmos. Chem. Phys.*, 18, 16461–16480, doi:10.5194/acp-18-16461-2018, 2018b.
- 1320 Takahashi, T., Nagao, Y. and Kushiyama, Y.: Possible High Ice Particle Production during



- 1321 Graupel–Graupel Collisions, *J. Atmos. Sci.*, 52, 4523–4527, 1995.
- 1322 Thompson, G., Rasmussen, R. M. and Manning, K.: Explicit Forecasts of Winter Precipitation
1323 Using an Improved Bulk Microphysics Scheme. Part I: Description and Sensitivity
1324 Analysis, *Mon. Weather Rev.*, 132, 519–542, doi:10.1175/1520-
1325 0493(2004)132<0519:EFOWPU>2.0.CO;2, 2004.
- 1326 Vali, G., Leon, D. and Snider, J. R.: Ground-layer snow clouds, *Q. J. R. Meteorol. Soc.*,
1327 138(667), 1507–1525, doi:10.1002/qj.1882, 2012.
- 1328 Vardiman, L.: The Generation of Secondary Ice Particles in Clouds by Crystal–Crystal
1329 Collision, *J. Atmos. Sci.*, 35, 2168–2180, doi:10.1175/1520-
1330 0469(1978)035<2168:TGOSIP>2.0.CO;2, 1978.
- 1331 Vignon, É., Alexander, S. P., DeMott, P. J., Sotiropoulou, G., Gerber, F., Hill, T. C. J.,
1332 Marchand, R., Nenes, A. and Berne, A.: Challenging and Improving the Simulation of
1333 Mid-Level Mixed-Phase Clouds Over the High-Latitude Southern Ocean, *J. Geophys. Res.*
1334 *Atmos.*, 126(7), 1–21, doi:10.1029/2020jd033490, 2021.
- 1335 Vionnet, V., Guyomarc’h, G., Naaim Bouvet, F., Martin, E., Durand, Y., Bellot, H., Bel, C.
1336 and Puglièse, P.: Occurrence of blowing snow events at an alpine site over a 10-year
1337 period: Observations and modelling, *Adv. Water Resour.*, 55, 53–63,
1338 doi:10.1016/j.advwatres.2012.05.004, 2013.
- 1339 Vionnet, V., Martin, E., Masson, V., Guyomarc’H, G., Naaim-Bouvet, F., Prokop, A., Durand,
1340 Y. and Lac, C.: Simulation of wind-induced snow transport and sublimation in alpine
1341 terrain using a fully coupled snowpack/atmosphere model, *Cryosphere*, 8(2), 395–415,
1342 doi:10.5194/tc-8-395-2014, 2014.
- 1343 Willmott, C. J., Robeson, S. M. and Matsuura, K.: A refined index of model performance, *Int.*
1344 *J. Climatol.*, 32(13), 2088–2094, doi:10.1002/joc.2419, 2012.
- 1345 Xu, L., Russell, L. M., Somerville, R. C. J. and Quinn, P. K.: Frost flower aerosol effects on
1346 Arctic wintertime longwave cloud radiative forcing, *J. Geophys. Res. Atmos.*, 118(23),
1347 13282–13291, doi:10.1002/2013JD020554, 2013.
- 1348 Yano, J. I. and Phillips, V. T. J.: Ice-Ice collisions: An Ice multiplication process in atmospheric
1349 clouds, *J. Atmos. Sci.*, 68(2), 322–333, doi:10.1175/2010JAS3607.1, 2011.
- 1350 Yano, J. I., Phillips, V. T. J. and Kanawade, V.: Explosive ice multiplication by mechanical
1351 break-up in ice-ice collisions: A dynamical system-based study, *Q. J. R. Meteorol. Soc.*,
1352 142(695), 867–879, doi:10.1002/qj.2687, 2016.
- 1353 Young, G., Lachlan-Cope, T., O’Shea, S. J., Dearden, C., Listowski, C., Bower, K. N.,
1354 Choularton, T. W. and Gallagher, M. W.: Radiative Effects of Secondary Ice Enhancement



1355 in Coastal Antarctic Clouds, *Geophys. Res. Lett.*, 46, 2312–2321,
1356 doi:10.1029/2018GL080551, 2019.

1357 Zhao, X. and Liu, X.: Global Importance of Secondary Ice Production, *Geophys. Res. Lett.*,
1358 doi:10.1029/2021GL092581, 2021.

1359 Zhao, X., Liu, X., Phillips, V. T. J. and Patade, S.: Impacts of secondary ice production on
1360 Arctic mixed-phase clouds based on ARM observations and CAM6 single-column model
1361 simulations, *Atmos. Chem. Phys.*, 21(7), 5685–5703, doi:10.5194/acp-21-5685-2021,
1362 2021.